



Honorary Degrees and Awards Committee
New Mexico Tech
Socorro, NM

April 9, 2016

Dear Honorary Degrees and Awards Committee,

I am pleased to nominate “Diagnosing DYNAMO convection with weak temperature gradient simulations,” by Stipo Sentic, Sharon Sessions, and Zeljka Fuchs, for consideration for the Langmuir award (best published paper by a graduate student). Physics graduate student Stipo Sentic was the lead in both the research and the writing of this paper.

This paper was published in the *Journal for Advances in Modeling Earth Systems (JAMES)*, and was **selected as a Research Spotlight by the Editor** and featured in *Eos*, the newsletter for the American Geophysical Union. According to the *Eos* Senior Editor’s assistant,

Research Spotlights summarize the research and findings of the best accepted articles for the broad Earth and space science community. Research Spotlights also may be sent to interested news media and may appear in the semi-monthly *Eos* magazine.

This is a prestigious distinction and a high honor, and is in alignment with the spirit of the Langmuir Award. The summary was published on both the *Eos.org* website, as well as part of the “Research Highlights” collection in *JAMES*. Both of these are included as part of this nomination.

This paper is significant to atmospheric and climate science because it addresses one of the most important, yet least well-understood sources of atmospheric variability: the Madden-Julian Oscillation (MJO). The MJO is a global scale disturbance that typically originates in the Indian Ocean, propagates slowly eastward with a signal that dissipates across the Pacific Ocean, but may reintensify back in the Indian Ocean after about 30 to 60 days. During its convectively active phase, it has a significant influence on weather and climate globally; despite its significance, the mechanisms responsible for initiating the MJO are still largely unknown.

In this paper, Mr. Sentic analyzed observational data taken from a 2011 field program, DYNAMO—Dynamics of the Madden-Julian Oscillation—and looked for relationships between diagnostic variables, including precipitation, moisture, and atmospheric stability. Identifying these relationships provides important information regarding potential mechanisms related to the control of the convection during the MJO. In addition to analyzing observations, Mr. Sentic performed several simulations using a cloud-system resolving model to determine whether these relationships were preserved in the simulations. Identifying and reproducing these relationships helps elucidate important causal mechanisms; in this work, Stipo hypothesized that some of the significant precipitation events observed during DYNAMO are the result of “balance dynamics”, which relates the dynamical state of the troposphere (specifically the vorticity or rotational signature) to the vertical temperature distribution. The convection, in turn, responds to the thermodynamic environment and produces the observed—and modeled—precipitation rates. This work has provided important clues not only regarding what we should look for in identifying causal mechanisms of the MJO, but what is needed for global models to accurately simulate the MJO and thus its effects.

JAMES is a significant journal of the American Geophysical Union (AGU). It has an impact factor of 4.92, which is one of the highest in comparison to other major journals, including: *Journal of Climate*, 4.44; *Journal of Atmospheric Sciences*, 3.14; *Geophysical Research Letters*, 4.20; and *Journal of Geophysical Research-Atmospheres*, 3.43.

The full citation for Mr. Sentic's paper is

Sentic, Stipo, Sharon L. Sessions, and Zeljka Fuchs (2015): Diagnosing DYNAMO Convection with Weak Temperature Gradient Simulations, *J. Adv. Model. Earth Syst.*, doi:10.1002/2015MS000531.

The *Eos Research Spotlight* and *JAMES Research Highlight* can be found at:

- <https://eos.org/research-spotlights/illuminating-the-controls-of-convection>
- <http://agupubs.onlinelibrary.wiley.com/agu/article/10.1002/2015MS000531/editor-highlight/>

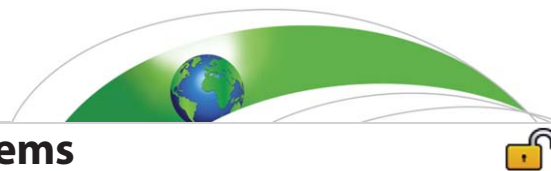
For convenience, I have included PDF copies of all of these to this nomination package.

In summary, this paper makes a very important contribution toward identifying important relationships between diagnostics in organized tropical convection. These are important for integrating into global weather and climate models, and this work has been recognized by the editors of the AGU journals as an important contribution. Although I provided guidance on the project, the work was all done by Mr. Sentic. It is an excellent paper and I strongly support it as a recipient of the Langmuir award.

Sincerely,



Sharon Sessions
Associate Professor
Department of Physics
New Mexico Tech
Socorro, NM 87801
sessions@kestrel.nmt.edu
(575)835-5798



RESEARCH ARTICLE

10.1002/2015MS000531

Diagnosing DYNAMO convection with weak temperature gradient simulations

Stipo Sentić¹, Sharon L. Sessions¹, and Željka Fuchs^{1,2}

Key Points:

- Relationships between convective diagnostics characterize DYNAMO convection
- WTG simulations reproduce observed diagnostic relationships
- GMS characterizes convective development and decay

Correspondence to:

S. Sentić,
ssentic@nmt.edu

Citation:

Sentić, S., S. L. Sessions, and Ž. Fuchs (2015), Diagnosing DYNAMO convection with weak temperature gradient simulations, *J. Adv. Model. Earth Syst.*, 07, doi:10.1002/2015MS000531.

Received 7 AUG 2015

Accepted 21 OCT 2015

Accepted article online 29 OCT 2015

¹Physics Department and Geophysical Research Center, New Mexico Institute of Mining and Technology, Socorro, New Mexico, USA, ²Department of Physics, Faculty of Science, Split, Croatia

Abstract Determining relationships between convective and environmental diagnostics can improve our understanding of mechanisms controlling tropical convection, and consequently, result in better representations of convection in coarsely resolved models. We identify important diagnostic relationships in observations taken during the Dynamics of the Madden-Julian Oscillation (DYNAMO) campaign and perform weak temperature gradient (WTG) simulations of DYNAMO convection to determine if the observed relationships are reproduced in our model. We find that the WTG approximation models local changes in the diagnostics used in the study—precipitation rate, atmospheric stability, moisture, and gross moist stability (GMS)—and reproduces diagnostic relationships suggested in previous studies; an increase in precipitation rate is correlated with increased atmospheric moisture content, which, in turn, is correlated with greater atmospheric stability. Large-scale atmospheric stability—changes of which might be related to balanced dynamics, we speculate—seems to be a candidate for a convective controlling mechanism. Observed and modeled interactions of local convection with the large-scale environment—quantified by the GMS—are in agreement with the theory of Inoue and Back (2015b); the GMS increases from small, positive or negative, values during developing convection and further increases for decaying convection past a critical GMS found at peak precipitation rates, atmospheric stability, and moisture content. Understanding the link between the critical GMS and the diagnostics—still a standing problem—could further our understanding of interactions between local convection and the large-scale environment.

1. Introduction

The Madden Julian Oscillation (MJO) [Madden and Julian, 1972] regulates weather and climate [Zhang, 2013] on both short time scales—precipitation, tornadoes, floods, fires, lightning, tropical cyclones, etc.—and long time scales—surface temperatures, extratropical climate modes, ENSO, Indian Ocean dipole, etc. Current weather and climate prediction models do not capture the MJO adequately [Kim et al., 2014; Benedict et al., 2014], in part because convective parameterizations are not properly modeling relationships between convection and the large-scale environment in which it is embedded. In order to improve our ability to model the MJO, and consequently the climate, we need to improve convective parameterizations. One way to do this is to improve our understanding of the relationships between convective processes and large-scale conditions.

Quantitative relationships between convective parameters and large-scale environmental conditions are a standing problem in modeling convection. For example, there is no consensus on the quantitative relationship between precipitation rate and moisture. Studies using satellite observations [Back and Bretherton, 2006; Peters and Neelin, 2006; Masunaga, 2012] and combined observation-numerical modeling studies [Raymond et al., 2007] have identified several forms of the precipitation rate-moisture relationship in the tropics; though they differ in detail, they all suggest that precipitation is a sensitive function of moisture. Studies have shown that general circulation models improve when precipitation rate depends on moisture quantity [Sherwood et al., 2010]. Further, both idealized numerical studies [Sessions et al., 2010, 2015] and numerical case studies [Wang et al., 2014] find that there is a relationship between the precipitation rate and the import or export of large-scale energy and moisture. Obtaining better diagnostic relationships among precipitation rate, moisture, and energy transport on the large scale—in the context of tropical convection—can improve parameterizations relevant to climate and weather predictions.

© 2015. The Authors.

This is an open access article under the terms of the Creative Commons Attribution-NonCommercial-NoDerivs License, which permits use and distribution in any medium, provided the original work is properly cited, the use is non-commercial and no modifications or adaptations are made.

To understand how tropical convection interacts with the large-scale environment, we model convection by parameterizing the large scale. One approach is to impose a mean, time-dependent, vertical velocity profile that is consistent with large-scale conditions in a model domain [Fridlind *et al.*, 2012; Woolnough *et al.*, 2010; Wang *et al.*, 2014] supplemented by horizontal temperature and moisture tendencies. This approach constrains the convection in a manner that reproduces the observed precipitation very closely. Problems, however, can arise in interpretation of results because imposing vertical motion constrains the precipitation and obscures causal mechanisms. More recent approaches do not specify the vertical motion but utilize an alternate parameterization of the large scale. Two examples are the weak temperature gradient (WTG) [Sobel and Bretherton, 2000; Raymond and Zeng, 2005] and the weak pressure gradient (WPG, also referred to as damped-gravity coupling, DGW) [Kuang, 2008; Romps, 2012a, 2012b] approximations. From these approximations, the vertical velocity is calculated from convection responding to observed large-scale conditions. The advantage of the WTG and WPG approximations is that the model convection is free to evolve and is not constrained by imposing tendencies of moisture and temperature.

A number of recent studies have used the WTG and WPG approximations to study convection in cloud resolving models (CRMs). In idealized WTG numerical simulations, researchers studied how convection responds to localized changes in sea surface temperatures (SST) [Sobel and Bretherton, 2000], surface fluxes and wind speed [Raymond and Zeng, 2005; Sessions *et al.*, 2010; Anber *et al.*, 2014], wind shear [Anber *et al.*, 2014], radiation [Anber *et al.*, 2015], and changes in atmospheric stability and moisture [Raymond and Sessions, 2007; Sobel and Bellon, 2009; Sessions *et al.*, 2015; Daleu *et al.*, 2015; Raymond *et al.*, 2015]. A recent study [Wang *et al.*, 2013] benchmarked how significantly the WTG and WPG approximations reproduced diagnostics in MJO convection of the Tropical Ocean Global Atmosphere Coupled Ocean Atmosphere Response Experiment (TOGA-COARE). A more recent study (Shuguang Wang *et al.*, Modeling the MJO in a cloud-resolving model with parameterized large-scale dynamics: Vertical structure, radiation, and horizontal advection of dry air, submitted to the *Journal of Advances in Modeling the Earth System*, 2015) revisited this in the context of the Dynamics of the Madden-Julian Oscillation (DYNAMO) field campaign [Johnson and Ciesielski, 2013; Ciesielski *et al.*, 2014a, 2014b; Johnson *et al.*, 2015] and also included comparison with a version of WTG that spectrally decomposes the heating anomaly (spectral WTG). So far, no study has compared observations and modeling results to determine if observed relationships between convective and environmental diagnostics are preserved in models; that is the goal of this paper.

We compare diagnostic relationships hypothesized to be relevant to tropical convection in observations and WTG simulations. We use observations from DYNAMO to force and verify WTG simulations. This work is similar to previous studies that implemented observations into WTG, spectral WTG, and WPG simulations [Wang *et al.*, 2013; Wang *et al.*, submitted manuscript, 2015]; those studies focused on the influences of different forcing mechanisms on local convection with different parameterizations of the large scale. However, there are some significant differences; not only do we perform WTG simulations with domain averages from DYNAMO North and South Sounding Arrays, we also force WTG simulations with individual DYNAMO station soundings in order to benchmark the WTG approximation in more localized conditions. The most important contribution of this work is a comparison between observed and modeled diagnostic relationships relevant to tropical dynamics. Identifying these relationships in observations is important for better understanding convection itself; determining whether these relationships are preserved in WTG experiments helps to validate the WTG approximation as a useful tool for understanding tropical convection.

This paper is organized as follows. In section 2, we describe the model, the WTG approximation, observations used in the study, and the methodology. In section 3, we compare observed and modeled diagnostic time series and relationships. In section 4, we present our conclusions, and in Appendix A, we present the details of verifying the modeled time series.

2. Model, Observations, and Methodology

In this section, we introduce the cloud resolving model (CRM), the WTG approximation, observations, and the methodology used in this study. The version of the WTG approximation we use is called the spectral weak temperature gradient approximation (SWTG) [Herman and Raymond, 2014] and is described in section 2.1.

2.1. Model and the Weak Temperature Gradient (WTG) Approximation

We use the CRM of *Herman and Raymond* [2014], which solves the fully compressible nonrotating momentum equations on a doubly periodic two-dimensional or three-dimensional domain. Prognostic equations govern specific moist entropy, the precipitation mixing ratio, and the total cloud water mixing ratio. The prognostic variable entropy is used because of improved conservation properties [*Raymond*, 2013] compared to the customary moist static energy. The dry (s_d), moist (s), and saturated (s^*) entropy are defined approximately as

$$s_d = c_p \ln \left(\frac{\theta}{\theta_R} \right), \quad (1)$$

$$s = c_p \ln \left(\frac{\theta_e}{\theta_R} \right), \quad (2)$$

$$s^* = c_p \ln \left(\frac{\theta_e^*}{\theta_R} \right). \quad (3)$$

Here c_p is the specific heat of dry air at constant pressure, $\theta_R = 300$ K is a reference temperature, and θ , θ_e , and θ_e^* are the potential, equivalent potential, and saturated equivalent potential temperatures, respectively. The model uses simplified microphysics and radiation [*Raymond*, 2001], and boundary layer turbulence is parameterized by Monin-Obukhov similarity theory. Please refer to *Herman and Raymond* [2014] for a detailed description of the model.

The CRM represents a limited region of the tropical atmosphere and interacts with a specified reference environment through the WTG approximation. The conventional WTG approximation is based on ideas from observations [*Bretherton and Smolarkiewicz*, 1989] and scaling arguments [*Charney*, 1963; *Sobel and Bretherton*, 2000] which indicate that gravity waves quickly redistribute heating anomalies, leaving weak horizontal temperature gradients in the tropics. Parcels with redistributed heat lift adiabatically and cool, equilibrating the system. In a model with periodic boundary conditions, like the one we are using, potential temperature anomalies due to latent heat release and radiative cooling are trapped in the domain. In order to mimic the real world process, the model generates a vertical velocity, called the WTG vertical velocity:

$$w_{wtg}(z, t) = \frac{D_\theta(z, t)M(z)}{\tau}, \quad (4)$$

where $D_\theta(z, t)$ —interpreted as the height a parcel needs to reach to remove a heating anomaly—is given by

$$D_\theta(z, t) = \frac{\bar{\theta}(z, t) - \theta_{ref}(z, t)}{\frac{\partial \bar{\theta}(z, t)}{\partial z}}. \quad (5)$$

Here $\bar{\theta}(z, t)$ is the domain averaged potential temperature, $\theta_{ref}(z, t)$ is the reference profile of potential temperature, τ is a relaxation time scale by which the model potential temperature is relaxed to the reference potential temperature, and $M(z) = \sin(\pi z/h)$ is a masking that modulates the enforcement of the WTG approximation to the region between the surface and the tropopause (h , assumed 15 km). The WTG velocity is interpolated from the boundary layer height (assumed 1 km) to zero at the surface. Also, the relaxation time scale, τ , can be interpreted as the time it takes gravity waves to travel the domain length and is taken to be 1 h in this study.

Recently, *Herman and Raymond* [2014] proposed a modification of this conventional WTG approximation which accounts for the fact that different heating profiles result in gravity waves of different speeds [*Bretherton and Smolarkiewicz*, 1989]. In contrast to the conventional WTG approximation—which assumes one phase speed for all wave numbers of buoyancy waves—the spectral WTG (SWTG) does a Fourier decomposition of the heating anomaly and assigns each wave number a corresponding phase speed:

$$c_j = N/m_j, \quad (6)$$

where N is the Brunt-Väisälä frequency and m_j is the vertical wave number mode. In SWTG, the equivalent height, $D_\theta(z, t)$ can be written as

$$D_{\theta}(z, t) = \sum_j \Theta_j(t) \sin(m_j z), \quad (7)$$

where

$$\Theta_j(t) = \frac{2}{h} \int_0^h D_{\theta}(z, t) \sin(m_j z) dz, \quad (8)$$

are the Fourier modes and h is the tropopause height. The SWTG vertical velocity can then be written as

$$w_{swtg}(z, t) = \sum_j \frac{\Theta_j(t)}{\tau_j} \sin(m_j z), \quad (9)$$

where

$$\tau_j = L/c_j = Lm_j/N = \pi Lj/hN, \quad (10)$$

is the relaxation time scale for each vertical wave number. In contrast to WTG where the user sets τ , the primary length scale L is the free parameter in SWTG, related to τ approximately by $L = \tau h N / \pi$. In this study, we will present SWTG simulations with $L = 171$ km, which is roughly equivalent to $\tau = 1$ h in the conventional SWTG. Henceforth, we will refer to the SWTG as WTG for convenience.

WTG sources of entropy and mixing ratio due to enforcing WTG are given by

$$S_{ent} = w_{wtg} \frac{\partial \bar{s}}{\partial z} + (\bar{s} - s_{ent}) \frac{1}{\rho_0} \frac{\partial \rho_0 w_{wtg}}{\partial z}, \quad (11)$$

$$S_{r_t} = w_{wtg} \frac{\partial \bar{r}_t}{\partial z} + (\bar{r}_t - r_{t-ent}) \frac{1}{\rho_0} \frac{\partial \rho_0 w_{wtg}}{\partial z}, \quad (12)$$

where ρ_0 is the domain average density, \bar{s} and \bar{r}_t are domain averaged moist entropy and total water vapor mixing ratio, and, depending on whether mass flux decreases with height (mass export) or increases with height (mass import):

$$S_{ent}, r_{t-ent} = \begin{cases} \bar{s}, \bar{r}_t & \text{if } \frac{\partial \rho_0 w_{wtg}}{\partial z} < 0 \text{ (mass export),} \\ S_{ref}, r_{t-ref} & \text{if } \frac{\partial \rho_0 w_{wtg}}{\partial z} > 0 \text{ (mass import),} \end{cases} \quad (13)$$

where S_{ref} and r_{t-ref} are reference profiles of moist entropy and water vapor mixing ratio. The WTG sources are used in the moist entropy and total water vapor mixing ratio equations to parameterize the effect of the environment on local modeled convection in the prognostic equations:

$$\frac{\partial \rho s}{\partial t} + \nabla \cdot (\rho \mathbf{v} s - K \nabla s) = \rho (S_{ss} + S_{sr} - S_{ent}), \quad (14)$$

$$\frac{\partial \rho r_t}{\partial t} + \nabla \cdot (\rho \mathbf{v} r_t - K \nabla r_t) = \rho (S_{rs} + S_{rp} - S_{r_t}), \quad (15)$$

where K is the eddy-mixing coefficient, \mathbf{v} is the velocity vector, S_{ss} and S_{sr} are the source of moist entropy from surface fluxes and radiation, respectively, S_{rs} is the total water vapor mixing ratio source due to surface fluxes, and S_{rp} is minus the conversion rate of cloud water to precipitation (details about these terms can be found in *Herman and Raymond [2014]*).

2.2. Observations and Diagnostic Variables

We use version 3a of the Colorado State University quality controlled observations from the DYNAMO field campaign [*Johnson and Ciesielski, 2013; Ciesielski et al., 2014a, 2014b; Johnson et al., 2015*]. We also use high-resolution radiosonde data from individual stations in the DYNAMO array (ARM AMF Radiosonde L3 Data for stations Male, Colombo, Gan, and Diego Garcia, and L3.1 for Research Vessels Reville and Mirai) [e.g., *Ciesielski et al., 2014a*], positions of which are shown in Figure 1. These observations are used for obtaining time-dependent reference profiles of potential temperature, mixing ratio, and surface winds which are used to force the WTG simulations (see below).

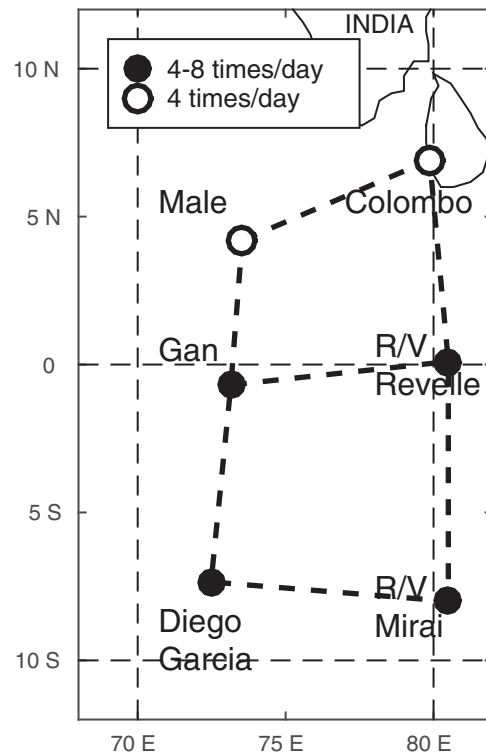


Figure 1. Station positions in the Dynamics of the Madden-Julian Oscillation (DYNAMO) campaign array.

of export of a quantity conserved in moist processes and import of a quantity that measures strength of convection (see Raymond et al. [2009], for a comprehensive overview of GMS). In this work, we calculated GMS from observations, Γ_{obs} , analogous to Sobel et al. [2014], as the ratio of moist and dry entropy divergence:

$$\Gamma_{obs} = \frac{\langle \omega \frac{\partial s}{\partial p} + \mathbf{v} \cdot \nabla s \rangle}{\langle \omega \frac{\partial s_d}{\partial p} \rangle}, \quad (17)$$

where ω is the vertical velocity in pressure coordinates and the brackets denote vertical pressure integral from surface to 100 hPa. Also, we neglect the horizontal part of dry entropy divergence as in Inoue and Back [2015a].

In calculating GMS from numerical output, the WTG velocity takes the place of large-scale vertical motion, and the lateral import or export of moist entropy and total mixing ratio is dependent on the layers where mass flux is positive or negative, respectively. The model GMS is defined as

$$\Gamma_{mod} = \frac{\langle S_{ent} \rangle}{\langle W_{wtg} \frac{\partial s_d}{\partial z} \rangle}, \quad (18)$$

where S_{ent} is the source of moist entropy due to the WTG approximation (equation (11)), and the brackets denote mass weighted height integral from the surface to the tropopause (15 km, around 100 hPa).

2.3. Methodology

We study the relationships between the observed and modeled DYNAMO diagnostics using the following procedure:

1. We run the model in non-WTG mode, with interactive radiation, until it reaches a state of radiative-convective equilibrium (RCE, i.e., convective forcing balances radiative cooling). For the RCE simulation, we use an SST of 302 K, which is the average SST in the DYNAMO intensive observation region (see below). We set the surface wind speed to 2 m s^{-1} , which is the average surface wind speed—here

The diagnostic variables we compare are precipitation rate, saturation fraction, instability index, and gross moist stability (GMS). These diagnostics provide important information about the relationships between convection and the environment and are significant in the context of the tropical atmosphere [Bretherton et al., 2004; Raymond et al., 2007; Raymond and Sessions, 2007; Gjorgjievska and Raymond, 2014; Sessions et al., 2015; Raymond et al., 2015]. Precipitation rate is a direct measure of convective activity, while saturation fraction—defined as precipitable water divided by saturated precipitable water—diagnoses the moistening effects of convection, with larger values corresponding to moister air columns. The instability index diagnoses the stability of air in the column. It is defined as [e.g., Raymond et al., 2011; Sessions et al., 2015]:

$$I = s_{low}^* - s_{high}^*, \quad (16)$$

where s_{low}^* and s_{high}^* are the horizontally averaged saturated moist entropy integrated from 1 to 3 km and 5 to 7 km, respectively. Smaller values of the instability index correspond to a more stable column of air.

Neelin and Held [1987] introduced the GMS as a variable that quantifies the relationship between convection and convective forcing in absence of the details of the nature of the relationship. GMS is defined as a ratio

defined as the wind speed at the lowest level—during DYNAMO, and run the model on a 2-D model domain 200 km long (1 km horizontal resolution) and 20 km high (250 m vertical resolution); the WTG simulations use the same model geometry as the RCE simulations. We obtain RCE potential temperature and total water mixing ratio profiles by averaging the last 30 days of a 50 day RCE simulation.

2. Observed potential temperature and mixing ratio anomalies, which represent changes in environmental conditions, are obtained by subtracting the time mean temperature and water vapor mixing ratio profile from the observational time series. We obtain anomalies for both DYNAMO array averaged profiles (North Sounding Array [NSA] and South Sounding Array [SSA]), and six individual sounding stations that compose NSA and SSA arrays (Male, Colombo, Gan, Diego Garcia, and Research Vessels *Revelle* and *Mirai*, see Figure 1 for positions). During port calls for *R/V Revelle* and *Mirai*, anomalies were set to zero (see Appendix A for details).
3. Finally, time-dependent reference profiles for WTG simulations are obtained by adding the observed DYNAMO potential temperature and water vapor mixing ratio anomalies (interpolated on the model grid) to the RCE profiles of potential temperature and mixing ratio.
4. In addition to the WTG reference profiles, observed surface wind speed and SST variations are imposed in the WTG simulations. For the NSA and SSA sounding arrays, daily SST variations are derived from ERA-I [Dee et al., 2011] since we lacked complete and representative surface observations [Wang et al., 2014]. Lacking SST observations for the single station simulations, we used an SST of 302 K (the average value from NSA and SSA derived from ERA-I). This treatment is justified since sensitivity studies (not shown) on NSA and SSA stations showed that removing or doubling SST variations did not have a significant impact on WTG results. Further, we do not consider the effects of shear and radiation in this study; we specify a noninteractive static cooling rate derived from the RCE simulation. Wang et al. (submitted manuscript, 2015) explore the impact of interactive radiative forcing compared to a static radiative cooling profile; although they find that interactive radiation is a significant source of moist static energy variations, we find that static radiative cooling is sufficient to reproduce variations in observed diagnostics. Further work is necessary to quantify the effects of radiation in our model.
5. We compare observed and modeled diagnostic time series, both qualitatively and quantitatively by computing statistical quantities such as correlation coefficients (with Student's *t* tests for significance levels), means, and standard deviations; these are presented in Appendix A. Since GMS is a sensitive variable, especially in numerical simulations, the time series data are smoothed with a 5 day moving average before daily averaging the time series; global characteristics of the diagnostics are preserved despite the loss in detail.
6. Finally, we compare relationships between diagnostic quantities for both observations and model results via a series of scatterplots.

3. Results and Discussion

In this section, we first compare time series in observed and modeled DYNAMO diagnostics. The time series were smoothed with a 5 day moving average in order to focus on large time scales and processes that influence the development of convection in DYNAMO [Sobel et al., 2014; Inoue and Back, 2015b]. Next, we compare observed and modeled diagnostic relationships and, where possible, compare them with past work. Here we do three sets of comparisons for each diagnostic relationship: observations with model, the NSA with the SSA, and arrays with the single stations. Details about time series for single station WTG simulations can be found in Appendix A.

3.1. Diagnostic Time Series

Figure 2 shows the NSA and the SSA observed (black) and modeled (red) time series of precipitation rate (a and b), saturation fraction (c and d), instability index (e and f), and GMS (g and h), smoothed with a 5 day moving average. Despite the applied smoothing, statistical relationships of interest in both observed and modeled time series are preserved. Also, after smoothing the GMS denominator and numerator, time periods where denominator is less than one fifth of the numerator have been removed, similar to Sobel et al. [2014], to avoid division by zero. For the reader's convenience, as rough guidelines, vertical dashed lines are aligned with precipitation maxima in the NSA, at days 25, 56, and 81.5. Despite the fact that precipitation maxima occur at different times for the NSA and the SSA, we use the NSA guidelines in the SSA plot for comparison.

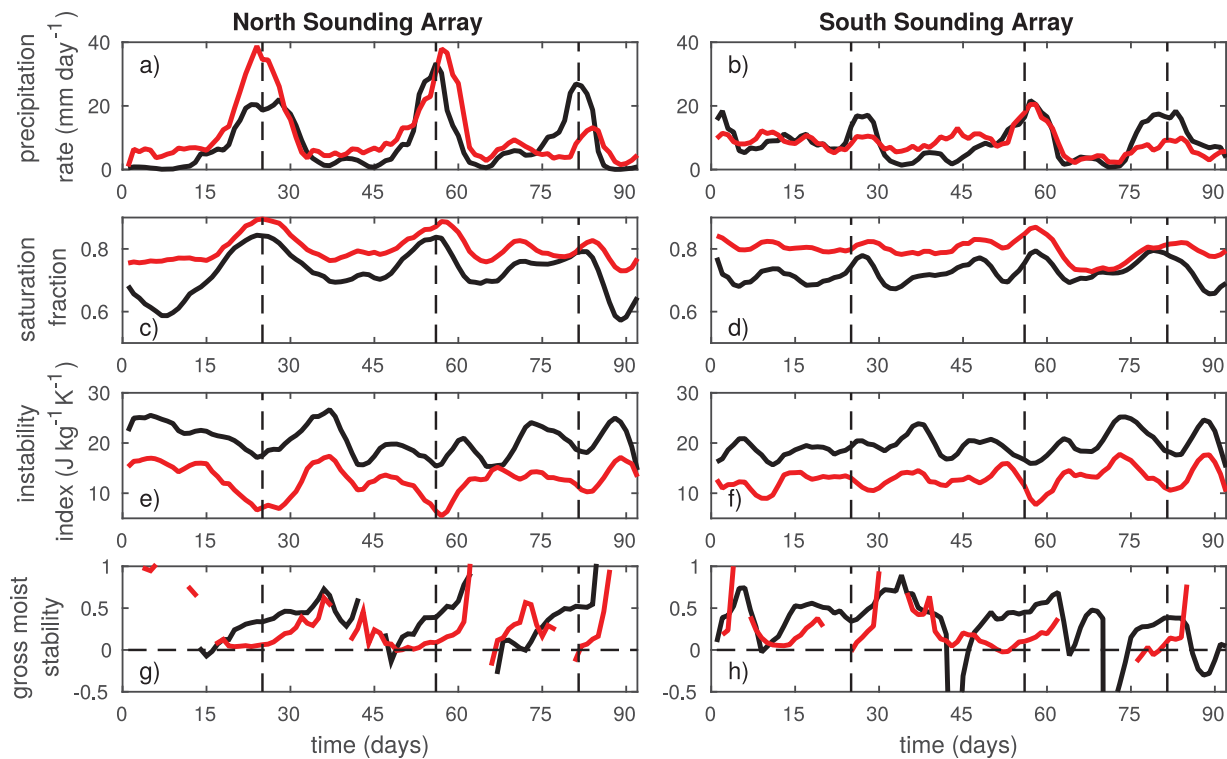


Figure 2. Smoothed (5 day moving average) time series of (a, b) precipitation rate, (c, d) saturation fraction, (e, f) instability index, and (g, h) gross moist stability (GMS), for observations (black) and weak temperature gradient simulations (red). The North Sounding Array (NSA) are on the left (Figures 2a, 2c, 2e, and 2g), and the South Sounding Array (SSA) are on the right (Figures 2b, 2d, 2f, and 2h). Vertical dashed lines are rough guidelines aligned with observed precipitation maxima in the NSA. For comparison, NSA guidelines are plotted on the SSA (Figures 2b, 2d, 2f, and 2h).

3.1.1. Comparison of Observations and Simulations

Figure 2 shows three distinct precipitation intense events—event being defined as the precipitation envelope comprising many individual convective events—around 25, 56, and 81.5 days for the NSA, all of which are approximately captured by the model. Compared to the NSA, the SSA has less intense precipitation rates with maxima that lag the NSA maxima for the first two events. The precipitation rate increase prior to the NSA precipitation maxima is correlated with an increase in saturation fraction and a decrease in instability index, both in observations and simulations (though the relationship is not equally strong for every precipitation event, see e.g., first event in the SSA). The inverse also holds for decreases of precipitation rate with time; after the precipitation maxima, the saturation fraction decreases and the instability index increases. This behavior is in agreement with a thermodynamic mechanism proposed in previous idealized WTG simulations and observations [Raymond and Sessions, 2007; Gjorgjievska and Raymond, 2014; Sessions et al., 2015; Raymond et al., 2011, 2014, 2015]. This mechanism posits that changes in the atmospheric stability—here stability is quantified via the instability index—result in changes to the convective profile, which in turn adjusts the vertical advection and lateral entrainment of moisture—here moisture in the column is quantified by saturation fraction. A decrease in the instability index (i.e., a more stable environment) causes more bottom heavy mass flux profiles which entrain moister lower-tropospheric air, and consequently increases the saturation fraction. An increased saturation fraction, in turn, results in higher precipitation rates, which has been confirmed in a number of studies [Bretherton et al., 2004; Raymond et al., 2007; Masunaga, 2012].

The saturation fraction and instability index peak and dip, respectively, in phase with peak precipitation rates, with significant differences in observed and modeled mean magnitudes. These differences could arise in part because of the RCE profiles used in the WTG reference profiles, and model parameters (e.g., dimensionality and microphysics), which the RCE profiles also depend on. The parameters used in the model [Raymond and Zeng, 2005] are, approximately, standard values found in the tropics, which might vary with geographic location. Alternatively, the model might be missing an essential mechanism for modeling

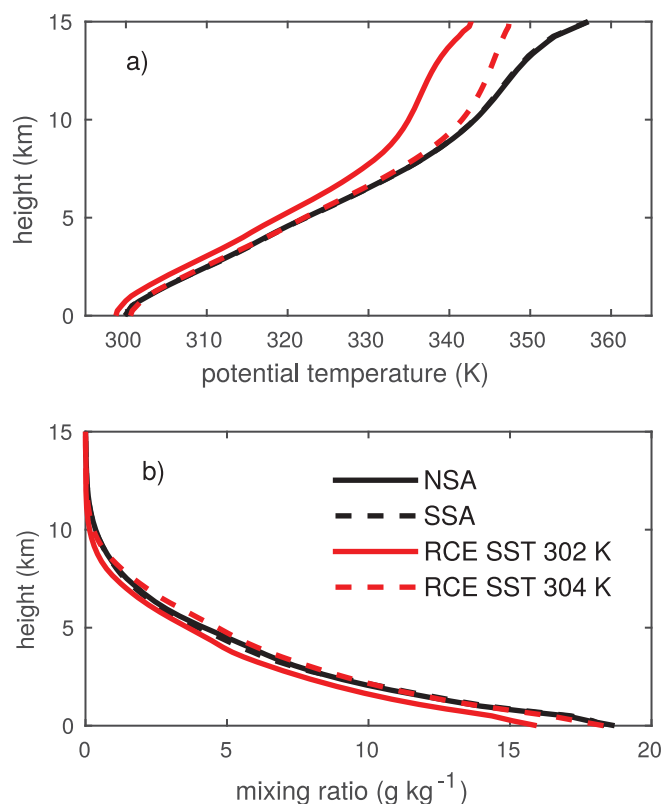


Figure 3. (a) Potential temperature and (b) water vapor mixing ratio, for the model radiative-convective equilibrium (RCE, red) and observations: North Sounding Array (NSA, solid black) and South Sounding Array (SSA, dashed black). Note that the NSA and the SSA curves overlap. The RCE mean profiles corresponding to mean observed SSTs are cooler and drier than the observed mean.

DYNAMO convection—possibly large-scale horizontal advection of dry air (see section 3.2, precipitation rate-instability index relationship). Here we restrict our discussion to the possible influence of the model setup to explain the discrepancy between observed and modeled saturation fraction and instability index, since possible mechanism deficiencies are beyond the scope of this study.

The discrepancy between observed and modeled saturation fraction and instability index might arise because of the RCE profiles used in the WTG reference profiles, which are computed using ERA-I SST averaged over the NSA and the SSA domains. However, model parameters and dimensionality of the computation domain [Wang and Sobel, 2011] influence significant differences between the RCE and observed mean potential temperature and moisture. Figure 3 shows the difference between the observed (black) and modeled (RCE, red) mean potential temperature (a) and water vapor mixing ratio (b). The RCE profile is cooler and shows a slightly smaller lapse rate than observations which

results in a smaller instability index compared to the observed mean profile. On the other hand, the RCE simulation is drier than the observed; the model, however, exhibits a higher saturation fraction in WTG simulations because the more stable RCE environment more efficiently entrains environmental air [Raymond and Sessions, 2007; Sessions et al., 2015]. Sensitivity studies (not shown) revealed that using RCE profiles of potential temperature and mixing ratio closer to the observed mean (e.g., using RCE profiles from SST of 304 K, shown with a red dashed line in Figure 3) decreases the difference between observed and modeled saturation fraction and instability index. However, the general results of this paper are not affected by this issue, and, for consistency, we choose to use the RCE profiles corresponding to the reanalysis SSTs.

Previous work [Johnson et al., 2015; Sobel et al., 2014] has addressed the energy budget in DYNAMO; Sobel et al. [2014] suggest that, compared to surface fluxes, the radiation might be more important in influencing the moist static energy budget during DYNAMO, and that horizontal advection plays an integral role in the second convective event. However, convection may evolve as a result of changes to the atmospheric stability, which may be a consequence of changes in radiation and surface fluxes, and—by modification of the convective profile—would influence the vertical and horizontal advection of moist static energy. Similarly, Inoue and Back [2015a] examined TOGA COARE data and found that vertical and horizontal advection of moist static energy is important for the development and decay of convection, and that radiation and surface fluxes act to destabilize convection throughout convective events. The effects of horizontal and vertical transport of convection can be summarized by the gross moist stability (GMS), and we address them next.

3.1.2. Gross Moist Stability (GMS)

GMS summarizes the effects of large-scale interactions on convection; understanding what controls GMS can lead to a better representation of convection in coarsely resolved models.

The observed GMS (Figures 2g and 2h) increases from small and even slightly negative values during developing convection (periods of increasing precipitation rate, prior to precipitation maxima on days 25,

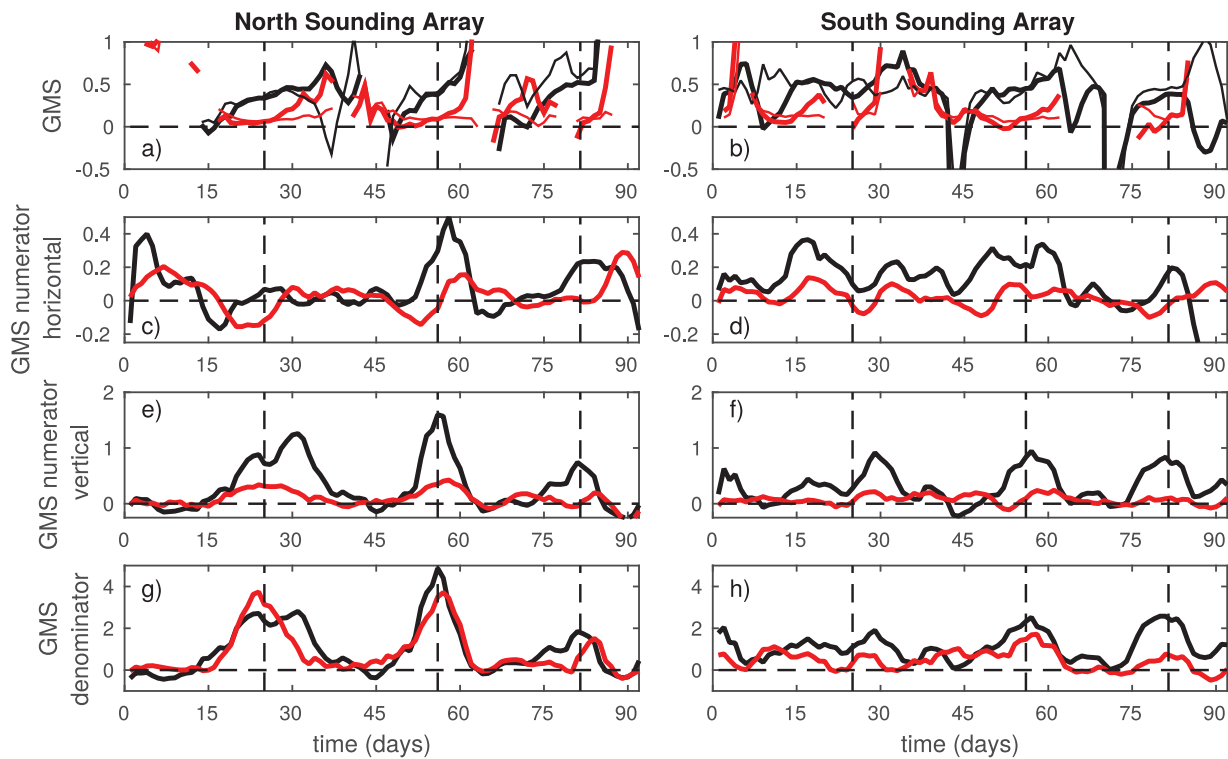


Figure 4. Smoothed (5 day moving average) time series of the (a, b) gross moist stability (GMS) and critical GMS (defined in equation (19), Figures 4a and 4b), (c, d) horizontal and (e, f) vertical components of the GMS numerator, and the (g, h) GMS denominator, for observations (black) and spectral weak temperature gradient simulations (red); for the North Sounding Array (NSA, Figures 4a, 4c, 4e, and 4g) and the South Sounding Array (SSA, Figures 4b, 4d, 4f, and 4h). Vertical dashed lines are rough guidelines aligned with observed precipitation maxima in the NSA. For comparison, NSA guidelines are plotted on the SSA (Figures 4b, 4d, 4f, and 4h).

56, and 81.5), and it continues to increase for dissipating convection (decreasing precipitation rate, after the precipitation maxima). The model GMS behaves similarly, but with a magnitude that is smaller than the observed at peak precipitation rates. Despite this difference in magnitude, the modeled GMS also shows an increase similar to the observed GMS, relative to the GMS values at peak precipitation rates; GMS increases throughout the life cycle of the convective event (which was also noted by *Sobel et al.* [2014]).

This GMS behavior has been addressed in a recent study. Based on TOGA-COARE data, *Inoue and Back* [2015a] developed a theory for convective development and decay relative to a critical GMS value:

$$\Gamma_c = \frac{\langle Q_R \rangle + \langle SF \rangle}{\langle \nabla \cdot (s_d \vec{v}) \rangle}, \quad (19)$$

where Q_R and SF are radiative and surface flux forcing, respectively, and $\nabla \cdot (s_d \vec{v})$ is the divergence of dry entropy. The authors show that convective development (precipitation increases with time) occurs for GMS values lower than Γ_c —which turns out to vary little with $\Gamma - \Gamma_c$ during TOGA COARE [*Inoue and Back*, 2015a]—while convective decay (precipitation decreases with time) happens for GMS values higher than Γ_c . This behavior can be seen for some of the convective events in Figures 4a and 4b, which shows the GMS (from Figures 2g and 2h, thick lines), and the critical GMS (Γ_c , thin lines) for the observations and the model; for comparison, the dashed vertical lines represent the NSA precipitation maxima. The model follows the theory and observations from *Inoue and Back* [2015a]; Γ_c remains fairly constant, and $\Gamma < \Gamma_c$ for developing modeled convection, and $\Gamma > \Gamma_c$ for decaying modeled convection. A particularly nice model example is seen on days 50–60. The observed Γ_c , on the other hand, deviates somewhat from the theory; at times the observed GMS is in phase with Γ_c , while at times it shows behavior opposite to that of *Inoue and Back* [2015a]. This discrepancy might be influenced by noise in the observational data, analysis of which is beyond the scope of this study.

In addition to the usefulness of the critical GMS time series in studying the dynamics of convection, calculating a critical value for a particular data set can also be useful. *Inoue and Back* [2015a] list several different

Table 1. Characteristic Gross Moist Stability^a (GMS)

Characteristic GMS (Γ_c)	Γ'_{\max}	$\tilde{\Gamma}'$	$\tilde{\Gamma}$	Γ_0
NSA observations	0.412	0.428	0.395	0.372
NSA SWTG	0.103	0.065	0.098	0.137
SSA observations	0.409	0.455	0.398	0.378
SSA SWTG	0.160	0.054	0.138	0.169

^aCharacteristic GMS calculated by all four methods listed by *Inoue and Back* [2015a], see text for definitions; values for the North Sounding Array (NSA) and South Sounding Array (SSA), for the observations, and spectral weak temperature gradient (SWTG) simulations. Γ'_{\max} is also shown in Figure 7.

methods for calculating the critical GMS found in the literature; here we redefine them in terms of moist entropy instead of moist static energy. According to *Inoue and Back* [2015a], the critical GMS can be calculated as follows:

1. GMS at maximum anomalous precipitation:

$$\Gamma'_{\max} \equiv \Gamma|_{p_{\max}}, \quad (20)$$

2. GMS computed from a scatterplot of anomalous $\nabla \cdot \langle s\mathbf{v} \rangle$ versus $\nabla \cdot \langle s_d\mathbf{v} \rangle$:

$$\tilde{\Gamma}' \equiv \frac{\overline{\langle \nabla \cdot \langle s\mathbf{v} \rangle \rangle' \cdot \langle \nabla \cdot \langle s_d\mathbf{v} \rangle \rangle'}}{(\overline{\langle \nabla \cdot \langle s_d\mathbf{v} \rangle \rangle'})^2}, \quad (21)$$

3. GMS computed from a scatterplot of nonanomalous $\nabla \cdot \langle s\mathbf{v} \rangle$ versus $\nabla \cdot \langle s_d\mathbf{v} \rangle$:

$$\tilde{\Gamma} \equiv \frac{\overline{\langle \nabla \cdot \langle s\mathbf{v} \rangle \rangle \cdot \langle \nabla \cdot \langle s_d\mathbf{v} \rangle \rangle}}{(\overline{\langle \nabla \cdot \langle s_d\mathbf{v} \rangle \rangle})^2}, \quad (22)$$

and

4. GMS in a quasi steady state:

$$\Gamma_0 \equiv \frac{\overline{\langle \nabla \cdot \langle s\mathbf{v} \rangle \rangle}}{\overline{\langle \nabla \cdot \langle s_d\mathbf{v} \rangle \rangle}}. \quad (23)$$

In this paper, we calculate the critical GMS, Γ_c , using each of these methods for both the NSA and the SSA in modeled and observed data. These results are shown in Table 1. Both the NSA and the SSA have critical GMS values close to 0.4, across all of the definitions. The modeled values, on the other hand, show more variability across the four definitions, and range from 0.1 to 0.2, with the SSA showing greatest range of variability compared to the NSA. We address the nontrivial difference between the observed and modeled critical GMS below, and in section 3.2.

The difference between the observed and modeled critical GMS values can be analyzed by decomposing the GMS into contributions from vertical, Γ_v , and horizontal, Γ_H , motions. To accommodate the coordinate systems of the observational and model data set, we have

$$\Gamma_{obs-v} = \frac{\langle \omega \frac{\partial s}{\partial p} \rangle}{\langle \omega \frac{\partial s_d}{\partial p} \rangle}, \quad (24)$$

$$\Gamma_{obs-H} = \frac{\langle \mathbf{v} \cdot \nabla s \rangle}{\langle \omega \frac{\partial s_d}{\partial p} \rangle}, \quad (25)$$

for the observations, and

$$\Gamma_{mod-v} = \frac{\langle W_{wtg} \frac{\partial s}{\partial z} \rangle}{\langle W_{wtg} \frac{\partial s_d}{\partial z} \rangle}, \quad (26)$$

$$\Gamma_{mod-H} = \frac{\langle (\bar{s} - s_{ent}) \frac{1}{\rho_0} \frac{\partial \rho_0 W_{wtg}}{\partial z} \rangle}{\langle W_{wtg} \frac{\partial s_d}{\partial z} \rangle}, \quad (27)$$

for the model (see term definitions in sections 2.1 and 2.2). Figures 4c–4f show the horizontal and vertical components of the GMS numerator; they differ in magnitude, both for the observations and the model. The

NSA horizontal transport of moist entropy (c) is about an order of magnitude smaller than the vertical transport (e) during intense precipitation periods; the difference is smaller for the SSA (d and f). This indicates the importance of the vertical transport in the development of convection in DYNAMO, and it is in agreement with *Inoue and Back* [2015a]. The source of the difference in the observed and the modeled GMS magnitudes seen in Figures 4a and 4b can be seen in Figures 4e and 4f; the model consistently underestimates the vertical transport of moist entropy compared to observed values.

The observed and modeled GMS denominator (Figures 4g and 4h) are in excellent agreement for the NSA, while it is generally slightly underestimated for the SSA. The success of the model in reproducing the denominator—the divergence of the dry entropy, $w_{wtg} \partial s_d / \partial z$ —is directly related to enforcement of the WTG approximation. In the WTG approximation, the vertical gradient of the dry entropy, $\partial s_d / \partial z$, is constrained explicitly by the relaxation of the temperature to the reference environment. The WTG vertical velocity, w_{wtg} , on the other hand, is not explicitly constrained and is calculated according to equation (4) or (9). Since the model captures the trends in the observed denominator, this indicates that the WTG approximation is adequately capturing the variations in the large-scale vertical velocity. On the other hand, the weaker denominator for the SSA indicates that the modeled SSA vertical advection is too weak and could possibly be adjusted by fitting the time scale τ or length scale L . The difference between the NSA and the SSA WTG simulations indicates differing dynamics in the two regions during DYNAMO; *Johnson and Ciesielski* [2013] show that the NSA was strongly modulated by the MJO, while the SSA also exhibited convection associated with both the MJO and the ITCZ. Our results suggest that the WTG approximation may be suitable for study of the MJO, because it performs better in the NSA, compared to the SSA where the ITCZ signal was strong.

3.1.3. Possible Sources of Stability Changes

So far our results suggest, in conjunction with previous work [*Raymond and Sessions*, 2007; *Sessions et al.*, 2015; *Raymond et al.*, 2015], that increased atmospheric stability (quantified by lower instability index) increases the moisture content (quantified by higher saturation fraction) and consequently increases the precipitation rate. Since the WTG simulations are forced by atmospheric stability changes—changes in the reference potential temperature profiles—the question of the sources of those changes arises.

In a recent paper, *Raymond et al.* [2015] develop a hypothesis relating the interplay of dynamics and thermodynamics in tropical convection. Given an evolution of the potential vorticity field with necessary boundary conditions and a balance condition—nonlinear balance, in case of the tropics—one could deduce the evolution of atmospheric stability, via changes to the virtual temperature (which are closely related to changes in potential temperature, e.g., see *Raymond et al.* [2014]). We do not know if this type of balanced dynamics is at work in DYNAMO, and although these data deserve a full analysis in this context, we present preliminary results which relate some of the diagnostics used from *Raymond et al.* [2015] to the dynamics in the DYNAMO. Specifically, we explore the possibility that there is a relationship among the vorticity, the divergence, and atmospheric stability in this case, as hypothesized for tropical convection [*Raymond et al.*, 2015].

Figure 5 shows time series of modeled divergence (a and b), budget derived [*Johnson and Ciesielski*, 2013; *Ciesielski et al.*, 2014a,b; *Johnson et al.*, 2015] divergence (c and d) and vorticity (e and f)—smoothed with a 5 day moving average—for the NSA and the SSA. The variables were averaged vertically in layers—0–15, 0–3, 3–8, and 8–15 km—in order to analyze the vertical structure of vorticity and divergence, and to speculate on possible correlation with stability changes. Despite the fact that the tropospheric vertical average from 0 to 15 km (black solid line) shows no features which might correlate with stability changes, significant patterns emerge when we divide the troposphere into layers.

Both for the NSA and the SSA, the divergence (Figures 5a–5d) shows strong positive values in the upper levels (8–15 km), signifying mass export, while weaker and negative values of divergence occur at midlevels (3–8 km) and low levels (0–3 km), signifying mass import. This pattern can be seen in both observed and modeled time series. The model differs from observations at midlevels (3–8 km) and shows weaker correlation with the observations in the SSA. Overall, the WTG approximation reproduces the DYNAMO divergence patterns, with deviations for the SSA.

The vorticity (e and f) distinguishes differing dynamics among the first, second, and third convective events both in the NSA and the SSA. In the NSA, the first event (days 15–35) shows little vortical activity during the

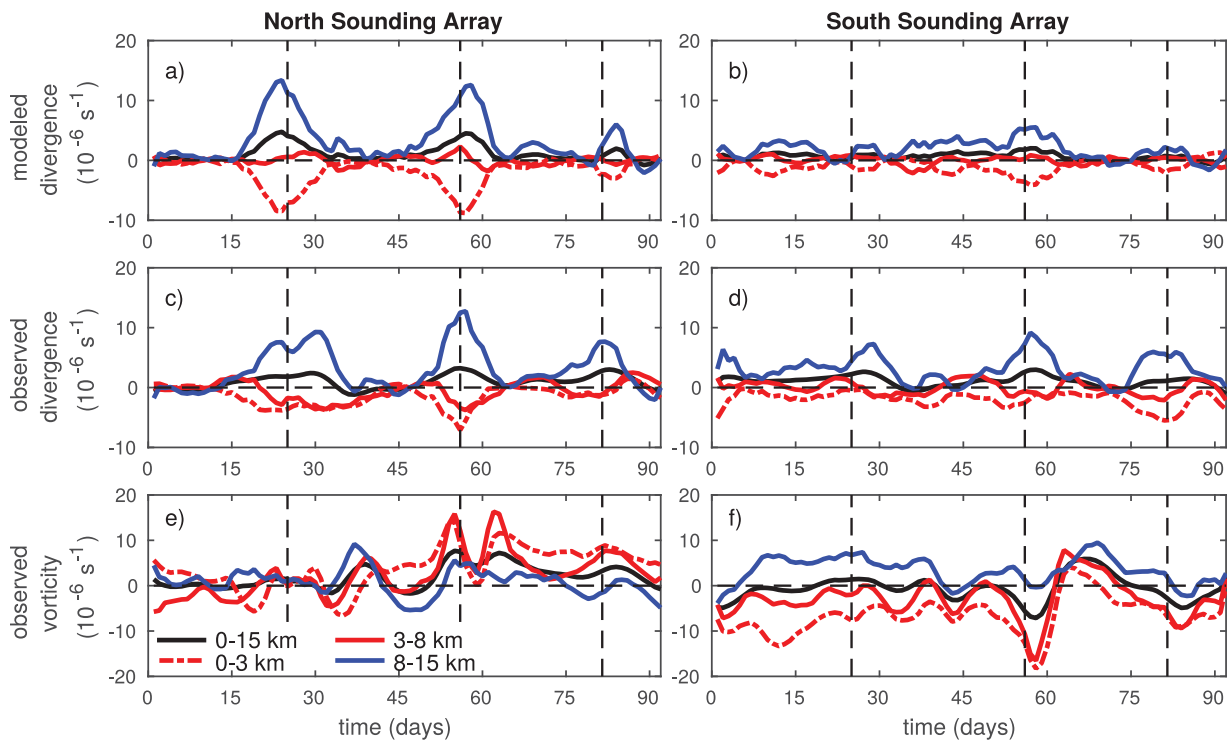


Figure 5. Time series of (a, b) modeled divergence, (c, d) observed divergence, and (e, f) observed vorticity for the North Sounding Array (NSA, Figures 5a, 5c, and 5e) and the South Sounding Array (SSA, Figures 5b, 5d, and 5f). Time series were smoothed with a 5 day moving average and averaged vertically in 0–15 km (solid black), 0–3 km (dashed red), 3–8 km (solid red), and 8–15 km (solid blue) layers. Vertical dashed lines are rough guidelines aligned with observed precipitation maxima in the NSA. For comparison, NSA guidelines are plotted on the SSA (Figures 5b, 5d, and 5f).

peak precipitation rate period from days 25 to 30. However, vorticity shows patterns during the developing (days 15–25) and decaying (days 30–35) phases of the first convective event. The vertical structure shows a dipole (negative vorticity at low levels and positive vorticity aloft) in the developing and the decaying phase. These vorticity features might be associated with stability changes during the development and decay of the first convective event, e.g., compare Figures 5e and 5f with Figures 2e and 2f. For the second NSA event (days 50–60), the low-level and midlevel vorticity show a prominent peak around the precipitation rate maximum, which could be associated with the atmospheric stability changes and convective development during that period. The second vorticity anomaly might be associated with a passing cyclone visible in infrared satellite imagery (not shown) [e.g., *Gottschalck et al.*, 2013]. The third precipitation event shows persistent surface vorticity with a developing midlevel vortex which peaks around the precipitation maximum. The low-level and midlevel vorticity is often stronger than the low-level and midlevel divergence, which might indicate a possible influence of balanced dynamics on the development and decay of the convective events. *Gottschalck et al.* [2013] showed that equatorial Rossby waves were active during DYNAMO in varying degrees, which further supports the possibility of balanced dynamics.

The SSA shows similar conditions with some major differences, apart from the fact that the SSA is on the southern hemisphere so that the vorticity bears, in general, the opposite sign compared to the NSA. The first precipitation event is accompanied by a persistent vorticity dipole from days 10 to 40. The constancy of this vorticity dipole might be associated with the moderate persistent precipitation rates from days 10 to 30, while the development of the midlevel vorticity around day 33 might be associated with decay of the convection. The second SSA precipitation event is associated with strong vorticity in low levels and midlevels, similar to the NSA. Last, the third precipitation event shows similar conditions as the NSA, with vorticity bearing the opposite sign.

In conclusion, we hypothesize that balanced dynamics might be associated with atmospheric stability changes during DYNAMO; distinct patterns observed in the DYNAMO vorticity field moves us to suggest this possibility. However, further work is necessary to test this hypothesis.

3.1.4. Individual Stations in the DYNAMO Array and WTG Verification

To obtain time series and verify the performance of the WTG approximation in simulating the convection during DYNAMO, we compared observed and modeled daily averaged time series of precipitation rate, saturation fraction, and instability index for WTG applied to individual stations in DYNAMO. It is useful to compare these with the results from the NSA and the SSA so that we have a measure for how well WTG performs using observations over different spatial scales. This result might help interpret WTG results from data taken from isolated soundings from field campaigns that do not have an ordered configuration of arrays like DYNAMO or TOGA COARE. A detailed account of the verification of WTG simulations on both station arrays (the NSA and the SSA), and individual stations, can be found in Appendix A.

In general, our comparisons of modeled and observed convective diagnostics for both regional arrays and single stations show that the WTG approximation qualitatively and quantitatively does a good job in reproducing the observed diagnostics with at least some of the differences accountable to the model parameters (e.g., microphysics and RCE profiles used in WTG reference profiles as explained above). There are some differences, however, that are not easily attributable to model parameters, which suggests that other mechanisms—one possibly being large-scale horizontal advection of dry air [Wang and Sobel, 2012; Wang et al., submitted manuscript, 2015]—which do not act through the thermodynamic environment are also important for modulating tropical convection. Although understanding what these are is important for improving convective parameterizations, a systematic analysis is beyond the scope of this study.

3.2. Diagnostic Relationships

In this section, we consider diagnostic relationships among precipitation rate, saturation fraction, instability index, and GMS. The relationship between these diagnostics has been studied in satellite observations as well as in models in past work. For example, Bretherton et al. [2004] and Raymond et al. [2007] have identified a strong relationship between precipitation rate and saturation fraction. Also, numerical studies by Raymond and Sessions [2007], Sessions et al. [2015], and Raymond et al. [2015] showed a strong dependence of the saturation fraction on the stability of the column air. We compare diagnostic relationships derived from observations and WTG simulations to see how significant the relationships are in observed data, and test if the WTG approximation preserves the diagnostic relationships. We do so for the NSA, the SSA, and all the results from the single station simulations.

Figure 6 shows observed (blue and black) and modeled (red) relationships between precipitation rate and saturation fraction (a–c), precipitation rate and instability index (d–f), and saturation fraction and instability index (g–i), for the NSA (a, d, and g), the SSA (b, e, and h), and the single station simulations (c, f, and i). We divided the observed data into two regimes because of distinctive behavior in observed relationships; events with precipitation rates lower than P_B and saturation fraction less than S_B (gray shaded area in a–c) are colored blue, while the remaining data are colored black. We choose $P_B = 5 \text{ mm d}^{-1}$, and $S_B = 0.73$ somewhat arbitrarily, but our choice does not qualitatively affect our results. We explain the reasons for this separation in detail below.

For qualitative comparison with previous research, we overlay the precipitation rate-saturation fraction functional relationships (Figures 6a–6c) from Bretherton et al. [2004, dashed blue]:

$$P(S) = \exp [b(S - S_D)], \quad (28)$$

where S is saturation fraction, and the numbers $b = 15.6$ and $S_D = 0.603$ are fitting parameters, and from Raymond et al. [2007, solid blue]:

$$P(S) = R_{RCE} * \frac{S_C - S_{RCE}}{S_C - S}, \quad (29)$$

where the number $S_C = 0.87$ is a fitting parameter, and $R_{RCE} = 4 \text{ mm d}^{-1}$ and $S_{RCE} = 0.81$ are steady state precipitation rate and saturation fraction for an RCE simulation. For the saturation fraction-instability index relationship (Figures 6g–6i), we overlay [Raymond et al., 2015, solid blue]:

$$S(I) = c * I + d, \quad (30)$$

where I is the instability index, and $c = -0.00433$ and $d = 0.897$ are fitting parameters. For quantitative comparison with previous work, we perform exponential and linear fits for the precipitation rate-saturation

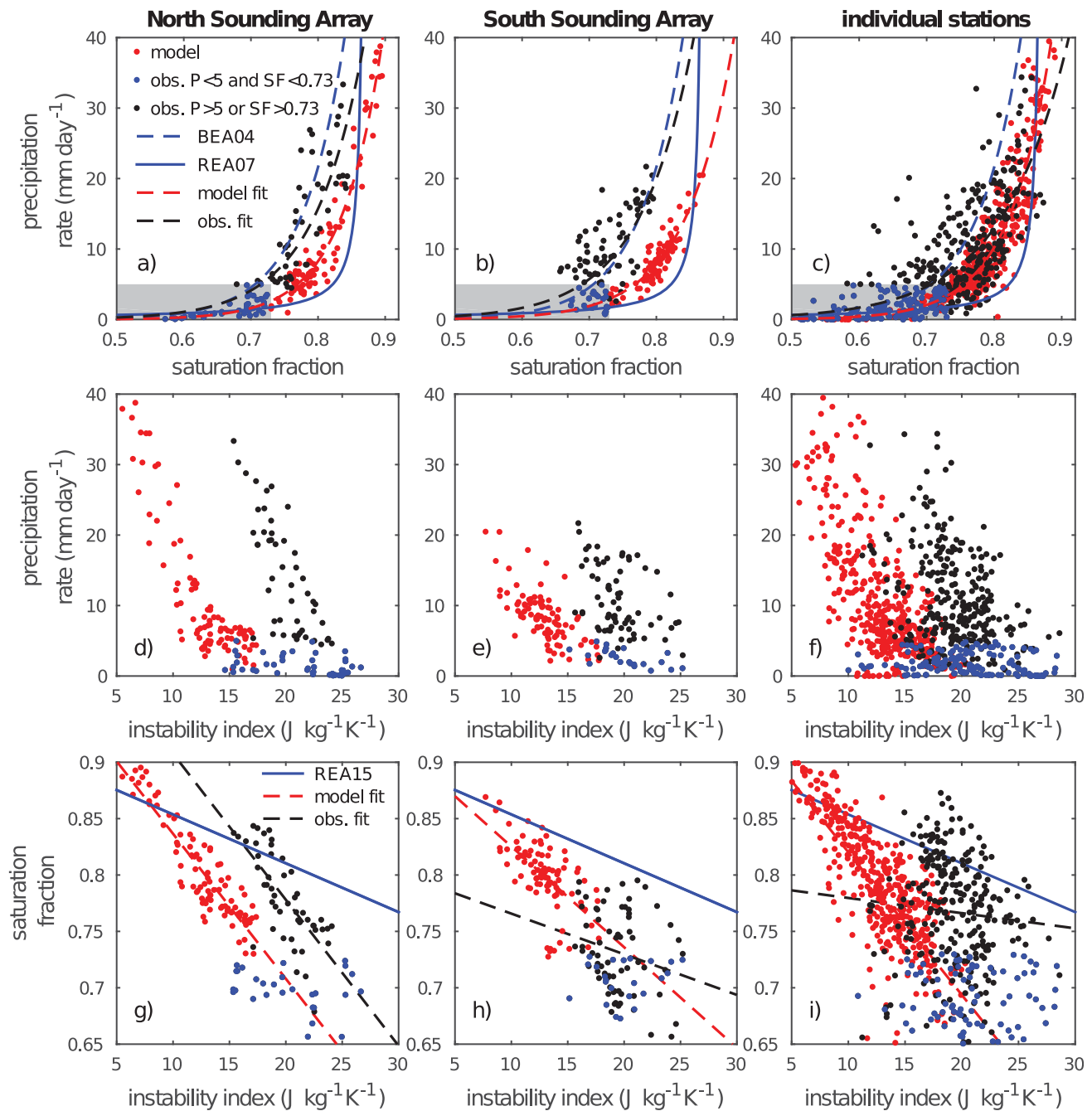


Figure 6. Relationships between (a–c) precipitation rate and saturation fraction, (d–f) precipitation rate and instability index, and (g–i) saturation fraction and instability index, for the North Sounding Array (NSA, Figures 6a, 6d, and 6g), South Sounding Array (SSA, Figures 6b, 6e, and 6h), and single station simulations (individual stations, Figures 6c, 6f, and 6i). Observations are shaded blue for precipitation rates and saturation fractions smaller than 5 mm d⁻¹ and 0.73 (gray shaded region in Figures 6a–6c), respectively, and black for the rest of the observed data, while the model is shaded in red. Precipitation rate–saturation fraction relationships from previous work are overlaid for comparison in the top row—dashed blue lines represents *Bretherton et al.* [2004] and solid blue represents *Raymond et al.* [2007]—while exponential fits for the DYNAMO observations and the model are the dashed black and red lines, respectively. The saturation fraction–instability index relationship from *Raymond et al.* [2015] has been overlaid for comparison in the bottom row—while linear relationship fits for the DYNAMO observations and the model are the dashed black and red lines, respectively. See Table 2 for details about the fits.

fraction and saturation fraction–instability index relationships, respectively, for the observations (dashed black curves) and model (dashed red curves). Table 2 lists the fit parameters with 95% confidence intervals, together with fit parameters for relationships from previous work for comparison.

Precipitation rate–saturation fraction relationship. The precipitation rate (Figures 6a–6c) increases with saturation fraction for both the average arrays and for all the single station simulations. The observed NSA and

Table 2. Diagnostic Relationship Fits^a

	Precipitation Rate-Saturation Fraction $P(S) = \exp[b(S - S_D)]$		Saturation Fraction-Instability Index $S(I) = c * I + d$	
	<i>b</i>	<i>S_D</i>	<i>c</i> (kg K J ⁻¹)	<i>d</i>
<i>Bretherton et al.</i> [2004]	15.6	0.603		
<i>Raymond et al.</i> [2015]			-0.0433	0.897
NSA	13.39 ± 1.96	0.59 ± 0.03	-0.013 ± 0.004	1.04 ± 0.07
	<i>16.36 ± 1.01</i>	<i>0.67 ± 0.01</i>	<i>-0.013 ± 0.01</i>	<i>0.97 ± 0.02</i>
SSA	12.47 ± 2.69	0.56 ± 0.04	-0.0036 ± 0.0038	0.80 ± 0.07
	<i>14.10 ± 1.31</i>	<i>0.65 ± 0.02</i>	<i>-0.0089 ± 0.0023</i>	<i>0.91 ± 0.03</i>
Single station simulations	10.4 ± 1.04	0.55 ± 0.02	-0.00118 ± 0.0021	0.79 ± 0.04
	<i>16.11 ± 0.62</i>	<i>0.66 ± 0.01</i>	<i>-0.012 ± 0.001</i>	<i>0.94 ± 0.02</i>

^aThe observational (roman) and model (italic) precipitation rate-saturation fraction and saturation fraction-instability index relationship fits, for the North Sounding Array (NSA), the South Sounding Array (SSA), and individual station simulations, compared to the relationships from previous work [*Bretherton et al.*, 2004; *Raymond et al.*, 2015].

SSA precipitation rate-saturation fraction scatters follow both the fit line (black dashed line) and the satellite observational fit from *Bretherton et al.* [2005, equation (28), blue dashed line], while the model scatter—and its exponential fit (red dashed line)—is closer to the *Raymond et al.* [2007, equation (29)] power law relationship; qualitatively, it seems that the modeled relationship might follow an exponential form. Quantitative conclusions on whether this relationship follows exponential or power law forms is beyond the scope of this study; the number of DYNAMO observations might be too small to make a statistically significant conclusion. Furthermore, the SSA relationships for both model and observations seem to follow the NSA relationships but do not extend to higher precipitation rates. It is interesting that the model effectively captures the general magnitude of the observed precipitation rates for all regions, but especially the differences in the NSA and the SSA. Indeed, fit parameters for the precipitation rate-saturation fraction relationship (Table 2) are similar for the NSA and the SSA, within variability, for both the observations and the model. In contrast to the NSA and the SSA, the single station observations and simulations show more scatter. One possible reason for less scatter in the NSA and SSA relationships might be the smoothing effect of the objective analysis used to interpolate data sets [*Johnson and Ciesielski*, 2013; *Ciesielski et al.*, 2014a] before they were averaged. Despite the scatter, however, the single station precipitation rate is a strong function of saturation fraction, similar to the NSA and the SSA, for both the observations and the model (Table 2 and Figures 6a–6c). This is the most important point of this result.

Both the model and observed data seem to have better fits to the exponential forms [*Bretherton et al.*, 2005, equation (28)] than to the inverse relation with the saturation deficit [*Raymond et al.*, 2007, equation (29)]. We note that the *Raymond et al.* [2007] relation was obtained from idealized steady state WTG simulations; deviations from this may arise as a result of transient dynamics. Furthermore, the NSA and the SSA observations are averaged over a larger area, similar to satellite measurements. Other studies with satellite data [*Masunaga*, 2012] have shown that the precipitation rate-saturation fraction relationship is time dependent, and that it is different for organized and unorganized convective regions.

Precipitation rate-instability index relationship. The precipitation rate increases with decreasing instability index (Figures 6d–6f) for the NSA, the SSA, and all the single stations. The NSA shows this prominently for both the observations and the model. However, the NSA also includes events with low precipitation rate for low instability index, which the model does not capture. These outliers fall into the region of precipitation rates lower than 5 mm d⁻¹ and saturation fractions lower than 0.73 (gray shaded region in Figures 6a–6c).

This behavior suggests that the WTG approximation does not capture a mechanism which inhibits precipitation events for increased stability (i.e., decreased instability index) of the outliers; one possible reason for this might be large-scale advection of dry air. As shown in equations (12) and (15), moisture in our model is based on lateral entrainment via mass conservation in the WTG velocity field [*Raymond and Zeng*, 2005; *Herman and Raymond*, 2014]. However, Wang et al. (submitted manuscript, 2015, Appendix A2) recently showed that the effects of large-scale horizontal transport of moisture are not fully captured by the entrainment formulation of the WTG approximation [*Raymond and Zeng*, 2005; *Herman and Raymond*, 2014]. This is evident in Figure A2 in Appendix A of the present paper; low saturation fraction periods—possibly caused by large-scale horizontal transport of dry air—are poorly captured. Despite the fact that the reference

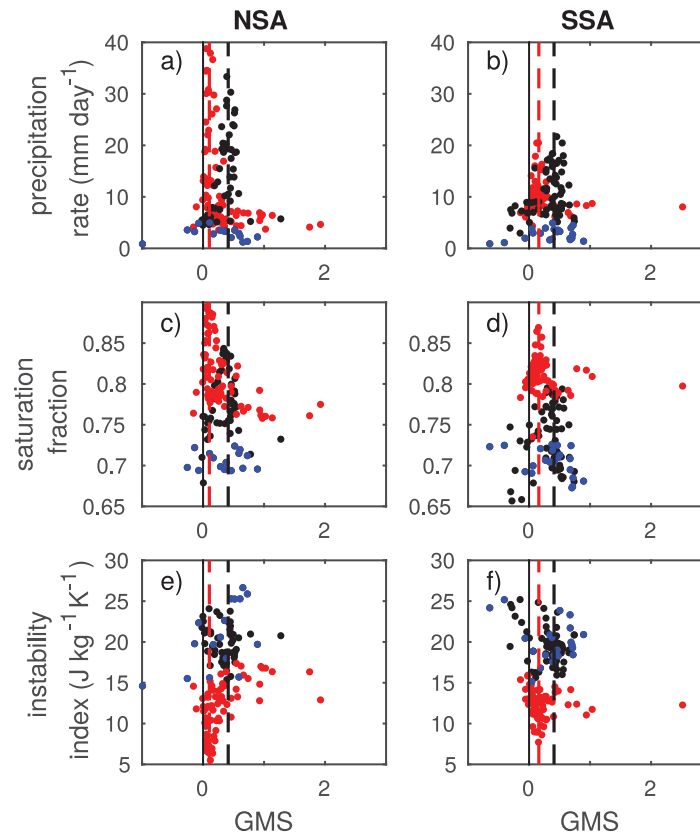


Figure 7. Relationships between the (a, b) precipitation rate and the gross moist stability (GMS), (c, d) saturation fraction and GMS, and (e, f) instability index and GMS, for the North Sounding Array (NSA, Figures 7a, 7c, and 7e), South Sounding Array (SSA, Figures 7b, 7d, and 7f). Observations are shaded blue for precipitation rates and saturation fractions smaller than 5 mm d^{-1} and 0.73, respectively, black for the rest of the observed data, while the model is shaded red. Vertical dashed lines represent the critical GMS value defined as the GMS at peak precipitation rates; black for observations (NSA 0.41, SSA 0.41) and red for the model (NSA 0.10, SSA 0.16). These critical GMS values are also listed in Table 1, as Γ'_{max} .

increases for lower instability index. A more stable atmosphere (quantified by a lower instability index) produces more bottom heavy mass flux profiles which entrain more moist air from the low levels [Raymond and Sessions, 2007; Raymond et al., 2011; Gjorgjievska and Raymond, 2014; Raymond et al., 2014; Sessions et al., 2015; Raymond et al., 2015]. This increases the saturation fraction, and consequently the precipitation rate (Figures 6a–6c). Data for low precipitation rates and low saturation fractions do not seem to follow this general trend (blue dots, Figures 6d–6f), perhaps because of dry air intrusion that decreases saturation fraction and therefore precipitation rates in more stable environments as suggested by Wang et al. (submitted manuscript, 2015), this, however, has not been tested.

Saturation fraction-instability index relationship. The saturation fraction, in general, increases with lower instability index (Figure 6g) in the NSA, both for the model and the observations. The outliers from the observed precipitation rate-instability index relationship were excluded before fitting a linear relationship on the data (Table 2) for comparison with the modeled relationship. The WTG approximation captures the observed strong dependence of saturation fraction on instability index for high saturation fraction events. For comparison, we overlaid the relationship from Raymond et al. [2015, solid blue], so far the only such relationship in the literature, which was derived for tropical cyclogenesis data for regions between 10° and 25° in the Pacific and North Atlantic (THORPEX Pacific Asian Regional Campaign, T-PARC, Tropical Cyclone Structure-08, TCS-08, and the Pre-Depression Investigation of Cloud-Systems in the Tropics, PREDICT), there is no a priori reason for it to hold at the equator, or to hold for the DYNAMO convection which might differ in controlling mechanisms. However, this comparison shows that the saturation fraction-instability index

profiles of the water vapor mixing ratio implicitly capture these dry periods, the model does not entrain the dry air due to export of moisture and moist entropy during suppressed periods. Also, it has been shown [Wang and Sobel, 2012] that entrainment of dry air has significant effects on precipitation rates and the vertical velocity in WTG simulations. This is a possible reason why our simulations exhibit stronger precipitation rates than observed in suppressed conditions.

We find similar behavior in the SSA though the relationship in the SSA is much less obvious owing to greater variability in atmospheric stability and lower observed precipitation values. Compared to the NSA and the SSA, the single station simulations also show more variance in atmospheric stability for low rain rates. Nevertheless, they still show a general increase in precipitation for more stable environments, consistent with the balanced dynamics hypothesis of Raymond et al. [2015].

As discussed in section 3.1.3, the balanced dynamics hypothesis explains how precipitation rate

relationship derived from DYNAMO data is a more sensitive function of the instability index than the cyclogenesis results from T-PARC, TCS-08, and PREDICT. It would be interesting to determine if this was a consequence of latitude or different dynamics related to cyclogenesis compared to the MJO.

The SSA observations (Figure 6h) differ from the NSA observations. There is more scatter in the SSA, and the outliers with precipitation rates lower than P_B and saturation fractions lower than S_B do not separate neatly; there are precipitation events greater than P_B for saturation fractions lower than S_B . This scatter produces a more uncertain slope for the SSA observational fit (Table 2, coefficient c for the SSA). The model fit, on the other hand, shows behavior similar to the NSA fit, with a slightly lower slope. The differences between the NSA and the SSA in all of the relationships so far, suggest a distinct feature; the WTG approximation seems to model the NSA region better than the SSA. The NSA experiences stronger precipitation rates which the WTG approximation captures, which might indicate that the WTG approximation works better in organized convection if we take the intensity of precipitation to be a measure of convective organization.

As expected, the single station observations (Figure 6i) show more scatter than the NSA and the SSA. Here similar to the SSA, the outliers with precipitation rates lower than P_B and saturation fractions lower than S_B exist for a wide range of the instability index. The scatter affects the linear fit for the observations in a similar manner as in the SSA; the correlation is weaker, and the slope is even lower than in the SSA. The scatter in the single station simulations might also reflect differences in local conditions for the individual stations.

Gross moist stability relationships. Given the existence of a critical GMS value related to peak precipitation rates [Inoue and Back, 2015a], we consider the relationship between the GMS and the precipitation rate, the saturation fraction, and the instability index. This can give us clues as to how the GMS is related to the convective development and decay in DYNAMO.

Figure 7 shows precipitation rate-GMS (a and b), saturation fraction-GMS (c and d), and instability index-GMS (e and f) relationships, for the NSA (a, c, and e) and the SSA (b, d, and f). We did not calculate the single station GMS relationships because it is impossible to calculate divergences for single point observed soundings. Also, the GMS for the WTG simulations of individual stations do not add any new information to the information from the WTG simulations of the NSA and the SSA (not shown). The scatterplot of precipitation rate and GMS shows the nonnegative critical GMS value—here defined as the value of GMS at maximum precipitation rate—in observations and simulations, both in the NSA and the SSA. We calculate the critical value as the average GMS for precipitation rates greater than 10 mm/d and mark it in the figure as a vertical dashed line (black for observations and red for model). This derived critical GMS value is also shown on remaining scatterplots in Figure 7 for comparison, for the NSA and the SSA, respectively. For comparison with Figure 6, events with precipitation rates less than P_B and saturation fractions less than S_B are shown in blue.

Although the precipitation-GMS relationship (a and b) is similar for the observations and the model; the critical GMS is different (0.41 for the observations and 0.1–0.2 for the model). One possibility for this discrepancy is a consequence of the difference between the observed and the modeled (RCE) mean potential temperature and mixing ratio used in the WTG simulations. However, preliminary sensitivity tests (not shown) reveal that using RCE profiles closer to the observed mean profiles do not significantly affect the modeled critical GMS. An alternative reason for the discrepancy might be a result of either the surface fluxes or the radiation, according to one definition of the critical GMS (equation (19)). Sensitivity simulations (not shown) indicate that radiation effects—adjusted by changing the strength of the imposed RCE radiative cooling profile—do not affect the value of the critical GMS; the divergence of dry entropy adjusts to preserve the critical GMS value of 0.1–0.2. Given that the reference thermodynamic environment and radiation do not seem to affect the critical value of the GMS, it would be interesting to further investigate what sets this critical value (e.g., surface fluxes, which we did not examine in sensitivity tests).

The saturation fraction-GMS (Figures 7c and 7d) and instability index-GMS (Figures 7e and 7f) relationships show behavior similar to the precipitation rate-GMS relationship. The peak saturation fraction and smallest instability index are aligned with the critical GMS value from peak precipitation rates (Figures 7a and 7b) both for the observations and the model, though the result is much stronger in the modeled convection. The instability index-GMS relationship (Figures 7e and 7f) is somewhat obscured by low precipitation rate and low saturation fraction events (shaded blue).

In conclusion, the critical GMS permeates the dynamics of convective development in the DYNAMO field campaign. We consider the instability index to be the independent variable in the WTG simulations: it is determined by the reference potential temperature profile, which in turn sets the convective profile which modulates the lateral import/export of moisture and moist entropy, thus controlling the saturation fraction, the GMS, and the precipitation rate. There is a strong relationship between the critical GMS and instability index, though further work is necessary to explain the link between the two.

4. Conclusions

In order to better understand how local convection interacts with large-scale conditions, we compared diagnostic relationships in observations and weak temperature gradient (WTG) simulations of Dynamics of the Madden-Julian Oscillation (DYNAMO) convection. First, we imposed observed variations of thermodynamic variables—potential temperature, water vapor mixing ratio, wind speed, and sea surface temperatures (SST)—in WTG simulations of the North Sounding Array (NSA), the South Sounding Array (SSA), and six individual stations from the DYNAMO campaign. By comparing precipitation rate, saturation fraction (which quantifies moisture content), and instability index (which quantifies atmospheric stability), we found that the model reproduces the observations reasonably well, both quantitatively and qualitatively, with some systematic differences. These differences are possibly attributable either to model parameters used to construct the WTG simulations or to dynamics that are not captured in the WTG approximation.

Second, we compared diagnostic relationships among the precipitation rate, the saturation fraction, the instability index, and the gross moist stability (GMS, which quantifies the interaction between local convection and large-scale conditions), in observations and simulations. We found the following:

1. The observed precipitation rate-saturation fraction relationship agrees with previous work [Bretherton *et al.*, 2004; Raymond *et al.*, 2004]: precipitation rate is a strong function of saturation fraction. The model shows similar behavior.
2. The observed and the modeled precipitation rate-instability index relationship agree and suggest that the precipitation rate is a sensitive function of atmospheric stability; a more stable environment (quantified by low instability index) precipitates more efficiently. Outliers to this relationship suggest that the WTG approximation does not capture dynamics which suppress precipitation in more stable environments which otherwise support strong precipitation. Alternatively, the relationship between precipitation rate and atmospheric stability occurs in more organized convection where the WTG approximation seems to perform well.
3. The observed and the modeled saturation fraction-instability index relationships also agree; though, more so for the NSA than the SSA and the individual stations in DYNAMO, which suggests different dynamics or perhaps different degrees of organization in the NSA compared to the SSA.
4. The relationships between the GMS and the precipitation rate, the saturation fraction, and the instability index show that the critical GMS value [Inoue and Back, 2015a] differs between the observations (0.41) and the model (0.1–0.2). However, the critical GMS value is ubiquitous to all of the diagnostics; maximum precipitation rates, saturation fractions, and minimum instability index values all occur at the critical GMS, both for the observations and the model.

Despite the differences in magnitudes, the modeled gross moist stability (GMS) captures the general characteristics of the observed GMS; in both the observations and simulations, the GMS goes from small and/or negative values in the developing stages of the convection, to larger positive values in the decaying phases of the strong convective events. In agreement with the theory of Inoue and Back [2015a], GMS smaller than the critical occurs during developing convection, GMS larger than the critical indicates decaying convection (at least in strong MJO events).

Combining the theory of Inoue and Back [2015a], and the effects of atmospheric stability on atmospheric moisture content and precipitation rates—described in section 3, and in Raymond and Sessions [2007], Sessions *et al.* [2015], and Raymond *et al.* [2015]—gives us a possible picture of how local convection interacts with large-scale changes observed during the DYNAMO campaign:

1. The stability of the environmental air sets the type of the convection, via the vertical structure of the mass flux profile; a more stable environment (quantified by lower instability index) produces more

bottom heavy mass flux profiles [Raymond and Sessions, 2007; Raymond et al., 2011, 2014; Gjorgjievska and Raymond, 2014; Sessions et al., 2015; Raymond et al., 2015].

2. During convective development, the mass flux profile influences the amount of moisture available for precipitation; a more bottom heavy mass flux profile vertically advects moister lower-tropospheric air while also importing more moist lower-tropospheric air via mass convergence at low levels [Raymond and Sessions, 2007]. The mass flux profiles in our WTG simulations are consistent with observed and are in agreement with previous studies (Wang et al., submitted manuscript, 2015, not shown).
3. Finally, the amount of moisture (quantified by saturation fraction) sets the precipitation rate since precipitation rate is a sensitive function of saturation fraction [Bretherton et al., 2004; Raymond et al., 2004].

This dynamical relationship has been demonstrated in observations of tropical cyclogenesis [Gjorgjievska and Raymond, 2014] but also seems to hold for the data presented here. This suggests, at least in strong (presumably more organized) convection, balanced dynamics also plays a role in the DYNAMO convection. A loose end in this study is the initial source of stability changes which eventually results in stronger precipitation rates. Raymond et al. [2015] indicates a potential vorticity anomaly is responsible for inducing the stability changes—further work, however, is necessary to study this possibility.

Appendix A: Verification of Weak Temperature Gradient Simulations

We verify the WTG simulations using reference profiles from individual stations, in addition to reference profiles derived from array averages (as a reminder, we use the spectral WTG approximation in these simulations). The combination of high-resolution radiosonde data and large-scale satellite derived precipitation rate, necessary for validating the WTG approximation on single stations, was not available until the DYNAMO campaign. Verifying the WTG approximation with precipitation gauge data is hindered by coarseness of precipitation gauge coverage. That is why we use Tropical Rainfall Measurement Mission (TRMM) data in tandem with DYNAMO sounding measurements for verifying both the sounding array and the single station simulations. The single station verification sets precedent for future studies for using the WTG simulations in cases where large arrays are not present, and only individual station soundings are available.

Figures A1, A2, and A3 show daily averaged observed and modeled precipitation rate, saturation fraction, and instability index, respectively, for NSA and SSA (a and b) and individual stations (c–h). Parts f and h also show periods (gray shading) when Research Vessels Revelle and Mirai were not present in their nominal positions; R/V Revelle was on-site from 4 October to 29 October, 10 November to 4 December, and 18 December to 31 December, while R/V Mirai was on-site (nominal position 80.5°E, 8°S) from 1 October to 24 October and 1 November to 27 November. During these periods the vessels were either traveling to the port or being stationed at the port—in which case the vessels did not collect data for those periods. During port calls, the observed anomalies were set to zero in WTG simulations, which was not done during the periods when the vessels traveled, i.e., we used observed anomalies even when the vessels were not on-site. Despite that, statistics were calculated only for on-site periods (noted above). Furthermore, correlation coefficients for each observation-model pair are also given. Table 1 lists the mean and standard deviation for all observed and modeled diagnostics with corresponding lag 0 correlation coefficients. Figure A1 also shows, in the subplot titles, the mean imposed wind speed with respective standard deviations, for comparison.

The NSA and the SSA precipitation rate (Figures A1a and A1b), saturation fraction (Figures A2a and A2b), and instability index (Figures A3a and A3b) are well reproduced, with SSA precipitation rate and saturation fraction having a weaker correlation with observations (Table 3). Modeled diagnostics for Male, Colombo, Gan, and Diego Garcia (Figures A1–A3, c–e and g) have a stronger correlation with observations than those for R/V Revelle and Mirai (Figures A1–A3, f and h; Table 3). Looking at differences between observed and modeled diagnostics, the model sometimes underestimates stronger precipitation rates for Gan and Diego Garcia (Figures A1–A3, e and g), which suggests that the WTG relaxation length scale (L) might depend on geographical location. The modeled precipitation rate at Male (Figure A1c) is stronger than the observed, and R/V Revelle and Mirai precipitation rates (Figures A1f and A1h) between the observations and the model are poorly correlated, possibly because the model imposed winds, which are derived from observations, are stronger than those at the other stations; surface fluxes might be overwhelming or amplifying

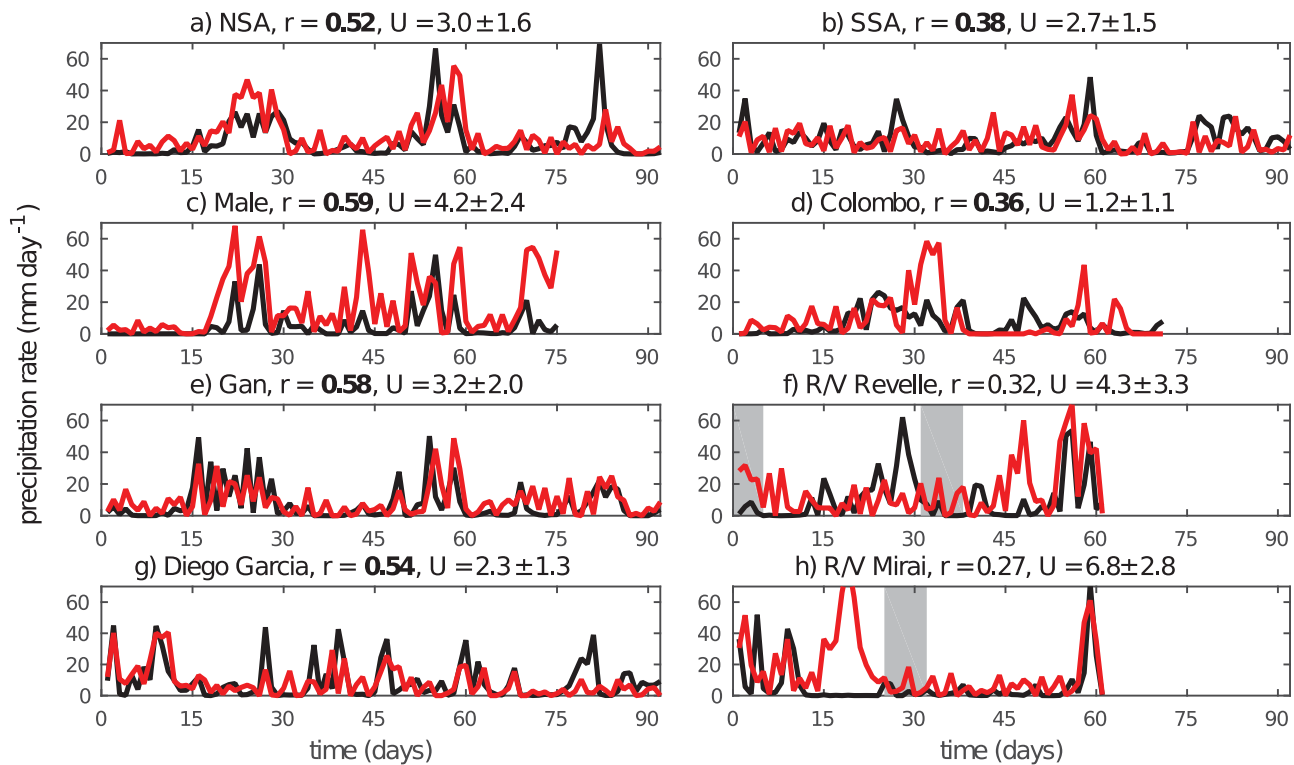


Figure A1. Observed (black) and modeled (red) daily precipitation rate time series for the (a) North Sounding Array (NSA), (b) South Sounding Array (SSA), and (c–h) individual stations from the Dynamics of the Madden-Julian Oscillation (DYNAMO) campaign. Gray shading represents periods when research vessels were not in their nominal positions; these periods were excluded for calculating statistics. Correlation coefficients (r) between the observations and the model significant to 98% are in bold. The mean and the standard deviation of surface wind speeds (U , in m s^{-1}) are also given, for comparison.

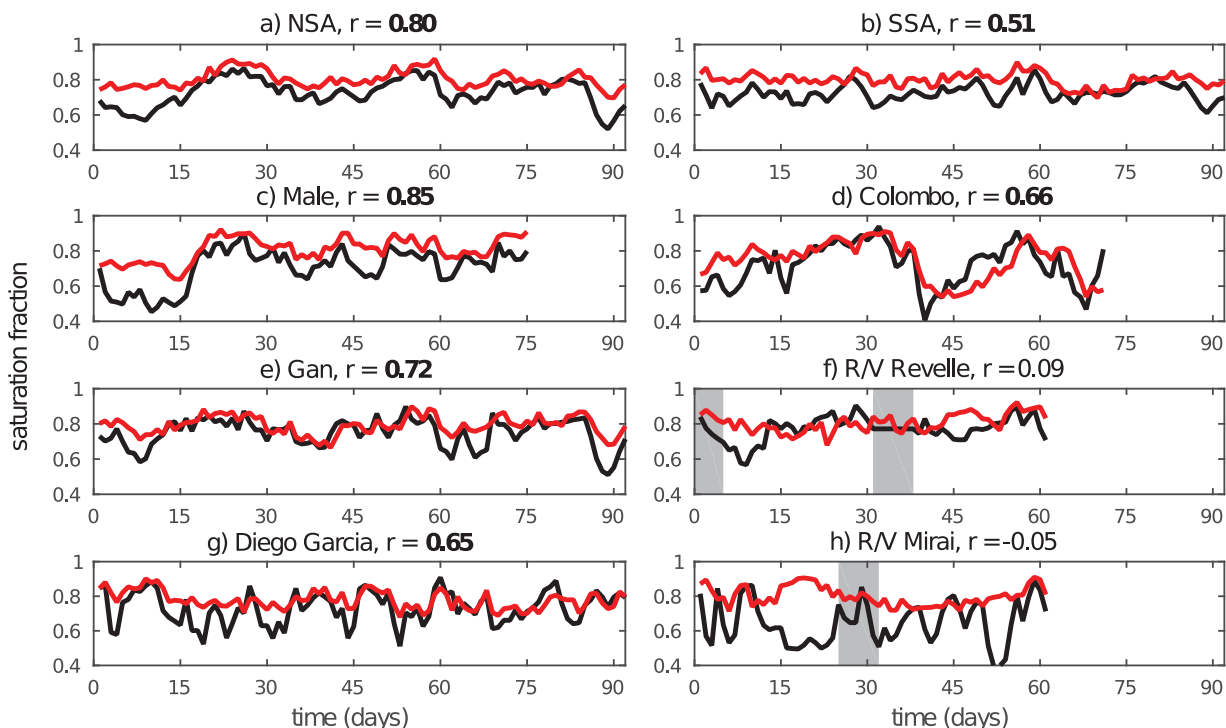


Figure A2. Same as Figure A1, but for the saturation fraction.

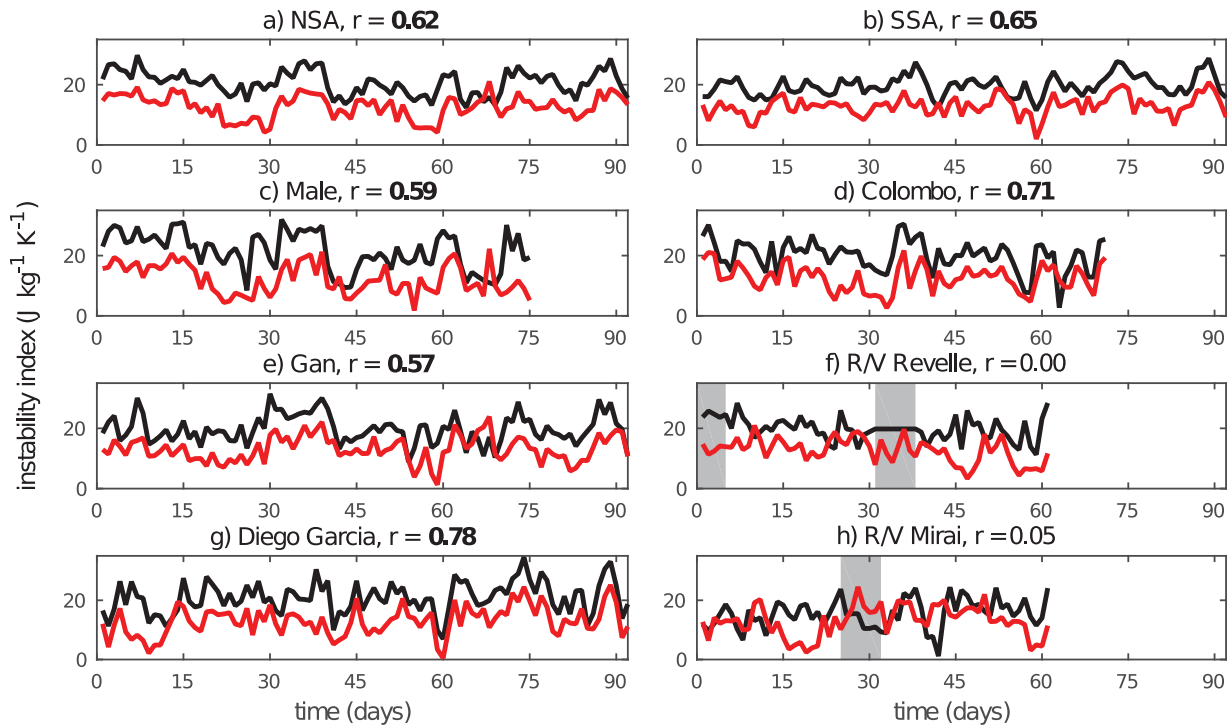


Figure A3. Same as Figure A1, but for the instability index.

WTG effects. Modeled saturation fraction and instability index are consistently larger and smaller, respectively, than observed; section 3.1.1 lists possible reasons for this discrepancy.

The poor correlation between observed and modeled diagnostics for stations R/V Revelle and Mirai (Figures A1–A3) might come from processes that cannot be captured by the WTG modeling paradigm. Qualitatively and quantitatively, the Mirai modeled precipitation rate (Figure A1h) follows observations well, except for a dry spell from days 15 to 25. A possible reason for the model missing the dry spell might be because the model did not capture the drying (seen in the saturation fraction, Figure A2) that lead to a nonprecipitating state from days 15 to 25. This drying may be a result of large-scale horizontal advection of dry air which is

Table 3. Modeled and Observed Statistics^a

	<i>N</i> (days)	Precipitation Rate (mm d ⁻¹)	<i>r</i>	Saturation Fraction (100%)	<i>r</i>	Instability Index (J kg ⁻¹ K ⁻¹)	<i>r</i>
NSA	92	8.4 ± 12.2	0.52	0.73 ± 0.08	0.80	20.6 ± 4.0	0.62
		<i>11.1 ± 12.4</i>		<i>0.80 ± 0.05</i>		12.7 ± 3.9	
SSA	92	8.7 ± 8.5	0.38	0.72 ± 0.05	0.51	19.7 ± 3.4	0.65
		<i>8.4 ± 7.3</i>		<i>0.80 ± 0.04</i>		12.9 ± 3.3	
Male	75	5.6 ± 9.9	0.59	0.70 ± 0.11	0.85	21.5 ± 6.3	0.59
		<i>18.6 ± 19.1</i>		<i>0.81 ± 0.07</i>		12.2 ± 5.0	
Colombo	71	6.6 ± 7.3	0.36	0.72 ± 0.12	0.66	20.0 ± 5.3	0.71
		<i>9.2 ± 13.9</i>		<i>0.74 ± 0.11</i>		12.6 ± 4.4	
Gan	92	7.5 ± 11.2	0.58	0.75 ± 0.08	0.72	19.7 ± 4.7	0.57
		<i>9.1 ± 9.8</i>		<i>0.79 ± 0.05</i>		13.1 ± 4.2	
R/V Revelle	49	11.7 ± 15.8	0.32	0.77 ± 0.08	0.09	19.5 ± 4.1	0.00
		<i>16.1 ± 18.3</i>		<i>0.81 ± 0.05</i>		12.5 ± 4.3	
Diego Garcia	92	9.1 ± 11.8	0.54	0.73 ± 0.09	0.65	20.8 ± 5.4	0.78
		<i>8.1 ± 9.5</i>		<i>0.78 ± 0.05</i>		13.0 ± 4.9	
R/V Mirai	53	6.7 ± 14.4	0.27	0.64 ± 0.13	-0.05	15.5 ± 5.0	0.05
		<i>17.0 ± 20.0</i>		<i>0.80 ± 0.06</i>		12.5 ± 5.2	

^aMean and standard deviation (observations roman, modeled italic), and lag zero correlation coefficients, *r*, between observed and modeled precipitation rate, saturation fraction, and instability index, for the DYNAMO North Sounding Array (NSA) and South Sounding Array (SSA), and individual stations. *N* is the number of daily averages in time series (sample size). Correlation coefficients significant at the 98% level are in bold.

not captured in the model (Wang et al., submitted manuscript, 2015). Modeled deep convective inhibition (DCIN, not shown)—defined as the average moist entropy from 0 to 1.75 km subtracted from the average saturated moist entropy from 1.75 to 2 km—had low values while the observed DCIN was substantial, which supports the hypothesis that the model did not capture the process leading to a dry state. R/V Revelle (Figure A1f) exhibits a similar behavior: after the first couple of days, the model misses the dry spell and goes into a state that does not resemble the observed. Further study is necessary to confirm the source of this behavior; these outliers, however, do not affect the conclusions of this paper.

Acknowledgments

We acknowledge Larissa Back and Shuguang Wang for insightful manuscript reviews. We thank Richard Johnson and Paul Ciesielski for the DYNAMO sounding and array data. We also thank David Raymond, Michael Herman, Patrick Haertel, and Larissa Back for fruitful discussions. We acknowledge high-performance computing support from Yellowstone (ark:/85065/d7wd3xhc) provided by NCAR's Computational and Information Systems Laboratory, sponsored by the National Science Foundation. The model data used in this study can be obtained by contacting the corresponding author (ssentic@nmt.edu). This work was supported by U.S. National Science Foundation grants ATM-1021049, ATM-1342001, and AGS-1056254.

References

- Anber, U., S. Wang, and A. Sobel (2014), Response of atmospheric convection to vertical wind shear: Cloud-system-resolving simulations with parameterized large-scale circulation. Part I: Specified radiative cooling, *J. Atmos. Sci.*, *71*, 2976–2993, doi:10.1175/JAS-D-13-0320.1.
- Anber, U., S. Wang, and A. Sobel (2015), Effect of surface fluxes versus radiative cooling on tropical deep convection, *J. Atmos. Sci.*, *72*, 3378–3388, doi:10.1175/JAS-D-14-0253.1.
- Back, L. E., and C. S. Bretherton (2006), Geographic variability in the export of moist static energy and vertical motion profiles in the tropical pacific, *Geophys. Res. Lett.*, *33*, L17810, doi:10.1029/2006GL026672.
- Benedict, J. J., E. D. Maloney, A. H. Sobel, and D. M. W. Frierson (2014), Gross moist stability and MJO simulation skill in three full-physics GCMs, *J. Atmos. Sci.*, *71*(9), 3327–3349, doi:10.1175/JAS-D-13-0240.1.
- Bretherton, C. S., and P. K. Smolarkiewicz (1989), Gravity waves, compensating subsidence and detrainment around cumulus clouds, *J. Atmos. Sci.*, *46*, 740–759.
- Bretherton, C. S., T. Uttal, C. W. Fairall, S. E. Yuter, R. A. Weller, D. Baumgardner, K. Comstock, R. Wood, and G. B. Raga (2004), The EPIC 2001 stratocumulus study, *Bull. Am. Meteorol. Soc.*, *85*, 967–977, doi:10.1175/BAMS-85-7-967.
- Bretherton, C. S., P. N. Blossey, and M. Khairoutdivnov (2005), An energy-balance analysis of deep convective self-aggregation above uniform SST, *J. Atmos. Sci.*, *62*, 4273–4292, doi:10.1175/JAS3614.1.
- Charney, J. G. (1963), A note on large-scale motions in the tropics, *J. Atmos. Sci.*, *20*(6), 607–609, doi:10.1175/1520-0469(1963)020 < 0607: ANOLSM>2.0.CO;2.
- Ciesielski, P. E., et al. (2014a), Quality-controlled upper-air sounding dataset for DYNAMO/CINDY/AMIE: Development and corrections, *J. Atmos. Oceanic Technol.*, *31*(4), 741–764, doi:10.1175/JTECH-D-13-00165.1.
- Ciesielski, P. E., R. H. Johnson, K. Yoneyama, and R. K. Taft (2014b), Mitigation of Sri Lanka island effects in Colombo sounding data and its impact on DYNAMO analyses, *J. Meteorol. Soc. Jpn.*, *92*(4), 385–405, doi:10.2151/jmsj.2014-407.
- Daleu, C. L., et al. (2015), Intercomparison of methods of coupling between convection and large-scale circulation: I. Comparison over uniform surface conditions, *J. Adv. Model. Earth Syst.*, doi:10.1002/2015MS000468, in press.
- Dee, D. P., et al. (2011), The ERA-Interim reanalysis: Configuration and performance of the data assimilation system, *Q. J. R. Meteorol. Soc.*, *137*(656), 553–597, doi:10.1002/qj.828.
- Fridlind, A. M., et al. (2012), A comparison of TWP-ICE observational data with cloud-resolving model results, *J. Geophys. Res.*, *117*, D05204, doi:10.1029/2011JD016595.
- Gjorgjievska, S., and D. J. Raymond (2014), Interaction between dynamics and thermodynamics during tropical cyclogenesis, *Atmos. Chem. Phys.*, *14*, 3065–3082, doi:10.5194/acp-14-3065-2014.
- Gottschalck, J., P. E. Roundy, C. J. Schreck III, A. Vintzileos, and C. Zhang (2013), Large-scale atmospheric and oceanic conditions during the 2011–12 DYNAMO field campaign, *Mon. Weather Rev.*, *141*, 4173–4196, doi:10.1175/MWR-D-13-00022.1.
- Herman, M. J., and D. J. Raymond (2014), WTG cloud modeling with spectral decomposition of heating, *J. Adv. Model. Earth Syst.*, *6*, 1121–1140, doi:10.1002/2014MS000359.
- Inoue, K., and L. Back (2015a), Gross moist stability assessment during TOGA COARE: Various interpretations of gross moist stability, *J. Atmos. Sci.*, *72*, 4148–4166, doi:10.1175/JAS-D-15-0092.1.
- Inoue, K., and L. Back (2015b), Column-integrated moist static energy budget analysis on various time scales during TOGA-COARE, *J. Atmos. Sci.*, *72*(5), 1856–1871, doi:10.1175/JAS-D-14-0249.1.
- Johnson, R. P., P. Ciesielski, J. J. Ruppert, and M. Katsumata (2015), Sounding-based thermodynamic budgets for DYNAMO, *J. Atmos. Sci.*, *72*, 598–622, doi:10.1175/JAS-D-14-0202.1.
- Johnson, R. H., and P. E. Ciesielski (2013), Structure and properties of Madden-Julian oscillations deduced from DYNAMO sounding arrays, *J. Atmos. Sci.*, *70*(10), 3157–3179, doi:10.1175/JAS-D-13-065.1.
- Kim, D., et al. (2014), Process-oriented MJO simulation diagnostic: Moisture sensitivity of simulated convection, *J. Clim.*, *27*(14), 5379–5395, doi:10.1175/JCLI-D-13-00497.1.
- Kuang, Z. (2008), Modeling the interaction between cumulus convection and linear gravity waves using a limited-domain cloud system-resolving model, *J. Atmos. Sci.*, *65*, 576–591, doi:10.1175/2007JAS2399.1.
- Madden, R. A., and P. R. Julian (1972), Description of global-scale circulation cells in the tropics with a 40–50 day period, *J. Atmos. Sci.*, *29*, 1109–1123, doi:10.1175/1520-0469(1972)029 < 1109:DOGSCC>2.0.CO;2.
- Masunaga, H. (2012), Short-term versus climatological relationship between precipitation and tropospheric humidity, *J. Clim.*, *25*, 7983–7990, doi:10.1175/JCLI-D-12-00037.1.
- Neelin, J. D., and I. M. Held (1987), Modeling tropical convergence based on the moist static energy budget, *Mon. Weather Rev.*, *115*, 3–12, doi:10.1175/1520-0493(1987)115 < 0003:MTCBOT>2.0.CO;2.
- Peters, O., and J. D. Neelin (2006), Critical phenomena in atmospheric precipitation, *Nat. Phys.*, *2*, 393–396, doi:10.1038/nphys314.
- Raymond, D. J. (2001), A new model of the Madden-Julian oscillation, *J. Atmos. Sci.*, *58*(18), 2807–2819, doi:10.1175/1520-0469(2001)058 < 2807:ANMOTM>2.0.CO;2.
- Raymond, D. J. (2013), Sources and sinks of entropy in the atmosphere, *J. Adv. Model. Earth Syst.*, *5*(4), 755–763, doi:10.1002/jame.20050.
- Raymond, D. J., and S. L. Sessions (2007), Evolution of convection during tropical cyclogenesis, *Geophys. Res. Lett.*, *34*, L06811, doi:10.1029/2006GL028607.
- Raymond, D. J., and X. Zeng (2005), Modelling tropical atmospheric convection in the context of the weak temperature gradient approximation, *Q. J. R. Meteorol. Soc.*, *131*, 1301–1320, doi:10.1256/qj.03.97.

- Raymond, D. J., S. K. Esbensen, C. Paulson, M. Gregg, C. S. Bretherton, W. A. Petersen, R. Cifelli, L. K. Shay, C. Ohlmann, and P. Zuidema (2004), EPIC2001 and the coupled ocean-atmosphere system of the tropical east Pacific, *Bull. Am. Meteorol. Soc.*, *85*, 1341–1354, doi:10.1175/BAMS-85-9-1341.
- Raymond, D. J., S. L. Sessions, and Z. Fuchs (2007), A theory for the spinup of tropical depressions, *Q. J. R. Meteorol. Soc.*, *133*, 1743–1754, doi:10.1002/qj.125.
- Raymond, D. J., S. L. Sessions, A. H. Sobel, and Z. Fuchs (2009), The mechanics of gross moist stability, *J. Adv. Model. Earth Syst.*, *1*, 9, doi:10.3894/JAMES.2009.1.9.
- Raymond, D. J., S. L. Sessions, and C. L. Carrillo (2011), Thermodynamics of tropical cyclogenesis in the northwest Pacific, *J. Geophys. Res.*, *116*, D18101, doi:10.1029/2011JD015624.
- Raymond, D. J., S. Gjorgjievska, S. L. Sessions, and Z. Fuchs (2014), Tropical cyclogenesis and mid-level vorticity, *Aust. Meteorol. Ocean. J.*, *64*, 11–25.
- Raymond, D. J., Z. Fuchs, S. Gjorgjievska, and S. L. Sessions (2015), Balanced dynamics and thermodynamic constraints in the tropical troposphere, *J. Adv. Model. Earth Syst.*, *7*, 1093–1116, doi:10.1002/2015MS000467.
- Romps, D. M. (2012a), Weak pressure gradient approximation and its analytical solutions, *J. Atmos. Sci.*, *69*(9), 2835–2845, doi:10.1175/JAS-D-11-0336.1.
- Romps, D. M. (2012b), Numerical tests of the weak pressure gradient approximation, *J. Atmos. Sci.*, *69*(9), 2846–2856, doi:10.1175/JAS-D-11-0337.1.
- Sessions, S. L., S. Sugaya, D. J. Raymond, and A. H. Sobel (2010), Multiple equilibria in a cloud resolving model using the weak temperature gradient approximation, *J. Geophys. Res.*, *115*, D12110, doi:10.1029/2009JD013376.
- Sessions, S. L., M. J. Herman, and S. Sentic (2015), Convective response to changes in the thermodynamic environment in idealized weak temperature gradient simulations, *J. Adv. Model. Earth Syst.*, *7*, 712–738, doi:10.1002/2015MS000446.
- Sherwood, S. C., R. Roca, T. M. Weckwerth, and N. G. Andronova (2010), Tropospheric water vapor, convection, and climate, *Rev. Geophys.*, *48*, RG2001, doi:10.1029/2009RG000301.
- Sobel, A., S. Wang, and D. Kim (2014), Moist static energy budget of the MJO during DYNAMO, *J. Atmos. Sci.*, *71*(11), 4276–4291, doi:10.1175/JAS-D-14-0052.1.
- Sobel, A. H., and G. Bellon (2009), The effect of imposed drying on parameterized deep convection, *J. Atmos. Sci.*, *66*, 2085–2096, doi:10.1175/2008JAS2926.1.
- Sobel, A. H., and C. S. Bretherton (2000), Modeling tropical precipitation in a single column, *J. Clim.*, *13*, 4378–4392, doi:10.1175/1520-0442(2000)013<4378:MTPIAS>2.0.CO;2.
- Wang, S., and A. H. Sobel (2011), Response of convection to relative sea surface temperature: Cloud-resolving simulations in two and three dimensions, *J. Geophys. Res.*, *116*, D11119, doi:10.1029/2010JD015347.
- Wang, S., and A. H. Sobel (2012), Impact of imposed drying on deep convection in a cloud-resolving model, *J. Geophys. Res.*, *117*, D02112, doi:10.1029/2011JD016847.
- Wang, S., A. H. Sobel, and Z. Kuang (2013), Cloud-resolving simulation of TOGA-COARE using parameterized large-scale dynamics, *J. Geophys. Res. Atmos.*, *118*, 6290–6301, doi:10.1002/jgrd.50510.
- Wang, S., A. H. Sobel, F. Zhang, Y. Q. Sun, Y. Yue, and L. Zhou (2014), Regional simulation of the October and November MJO events observed during the CINDY/DYNAMO field campaign at gray zone resolution, *J. Clim.*, *28*, 2097–2119, doi:10.1175/JCLI-D-14-00294.1.
- Woolnough, S. J., et al. (2010), Modelling convective processes during the suppressed phase of a Madden-Julian oscillation: Comparing single-column models with cloud-resolving models, *Q. J. R. Meteorol. Soc.*, *136*, 333–353, doi:10.1002/qj.568.
- Zhang, C. (2013), Madden-Julian oscillation: Bridging weather and climate, *Bull. Am. Meteorol. Soc.*, *94*(12), 1849–1870, doi:10.1175/BAMS-D-12-00026.1.

Illuminating the Controls of Convection

Researchers compare observations and models of air circulation over the tropics to determine if simulations capture how the environment shapes convection.

Source: Journal of Advances in Modeling Earth Systems (JAMES)



The Madden-Julian Oscillation drives weather and climate as it circles the globe over the Pacific Ocean. But just how environmental conditions shape convection within the massive air circulation pattern is only now becoming clearer to scientists. Credit: [Daehyun Kim](#)

By Kate Wheeling © 11 February 2016

The Madden-Julian Oscillation (<https://www.climate.gov/news-features/blogs/enso/what-mjo-and-why-do-we-care>) (MJO) is a pattern of atmospheric circulation that drifts eastward across the tropics, circling the Earth every 30 to 60 days. The massive circulation cells of the MJO rise and fall, driving changes in short-term weather phenomena like clouds and rainfall that alter sea surface temperatures and other global climate trends as the circulation pattern traverses the Indian and Pacific Oceans.

Despite the outsized effect of the MJO on weather and climate, it's unclear if current models effectively simulate the phenomenon. This is largely because the relationship between the bounds of convection—the upward movement of air through the atmosphere—and environmental conditions is not well understood. Identifying the relationship between convection and the environment is critical for understanding the atmospheric process itself. And models must be able to capture the nature of that relationship in order to adequately predict convection and its downstream effects on weather and climate.

With an eye on precipitation rate, the moisture content of the air, and the stability of the atmosphere, Sentić et al. (<http://onlinelibrary.wiley.com/doi/10.1002/2015MS000531/full>) sought to determine how these environmental conditions influence convection and provide means for evaluating whether current climate models are able to capture their impact.

Using observations of tropical convection and environmental conditions from the Dynamics of the Madden-Julian Oscillation (DYNAMO) (https://www.eol.ucar.edu/field_projects/dynamo) field campaign, the team compared observed relationships between convection and the environment with a cloud-resolving model (<https://www.youtube.com/watch?v=chIzYtJxhc>)—a high-resolution simulation capable of capturing the life cycles of single clouds and entire cloud systems.

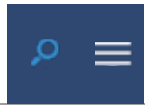
The study revealed that the model reasonably reproduced reality, providing the scientists with a clearer picture of MJO dynamics. On the basis of their findings, the authors suggest that the stability of the atmosphere sets the stage for convection. Then the flow of wet, humid air determines how much moisture is present for precipitation, which, in the end, determines the rate of rainfall.

The study is an important step in understanding the relationship between the environment and convection within the MJO—but the origin of the stability changes that set the process in motion, the authors note, is still a mystery. (*Journal of Advances in Modeling Earth Systems (JAMES)*, [doi:10.1002/2015MS000531](https://doi.org/10.1002/2015MS000531) (<http://onlinelibrary.wiley.com/doi/10.1002/2015MS000531/full>), 2015)

—Kate Wheeling, Freelance Writer

Citation: Wheeling, K. (2016), Illuminating the controls of convection, *Eos*, 97,
doi:10.1029/2016EO045429. Published on 11 February 2016.

© 2016. The authors. [CC BY-NC 3.0 \(https://creativecommons.org/licenses/by-nc/3.0/us/\)](https://creativecommons.org/licenses/by-nc/3.0/us/)



Highlights

Illuminating the Controls of Convection

The **Madden-Julian Oscillation (MJO)** is a pattern of atmospheric circulation that drifts eastward across the tropics, circling the Earth every 30 to 60 days. The massive circulation cells of the MJO rise and fall, driving changes in short-term weather phenomena like clouds and rainfall that alter sea surface temperatures and other global climate trends as the circulation pattern traverses the Indian and Pacific Oceans.

Despite the outsized effect of the MJO on weather and climate, it's unclear if current models effectively simulate the phenomenon. This is largely because the relationship between the bounds of convection—the upward movement of air through the atmosphere—and environmental conditions is not well understood. Identifying the relationship between convection and the environment is critical for understanding the atmospheric process itself. And models must be able to capture the nature of that relationship in order to adequately predict convection and its downstream effects on weather and climate.

With an eye on precipitation rate, the moisture content of the air, and the stability of the atmosphere, *Sentić et al.* sought to determine how these environmental conditions influence convection and provide means for evaluating whether current climate models are able to capture their impact.

Using observations of tropical convection and environmental conditions from the **Dynamics of the Madden-Julian Oscillation (DYNAMO)** field campaign, the team compared observed relationships between convection and the environment with a **cloud-resolving model**—a high-resolution simulation capable of capturing the life cycles of single clouds and entire cloud systems.

The study revealed that the model reasonably reproduced reality, providing the scientists with a clearer picture of MJO dynamics. On the basis of their findings, the authors suggest that the stability of the atmosphere sets the stage for convection. Then, the flow of wet, humid air determines how much moisture is present for precipitation, which, in the end, determines the rate of rainfall.

The study is an important step in understanding the relationship between the environment and convection within the MJO—but the origin of the stability changes that set the process in motion, the authors note, is still a mystery.

-- *Kate Wheeling, Freelance Writer, 4 February 2016*

RESEARCH ARTICLES

© 2016 American Geophysical Union

Diagnosing DYNAMO convection with weak temperature gradient simulations

Stjepan Seitić, Sharon L. Sessions, Željka Fuchs



AGU Publications

First Published: 19 November 2015 | Vol: 7, 1849–1871 | DOI: 10.1002/2015MS000531

AGU.org

[Open Access](#)

AGU Membership

Author Resources

Contact AGU

Editor Searches

Librarian Resources

Media Kits

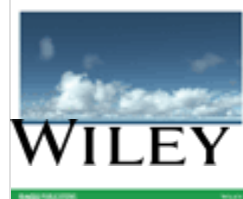
Publication Award

Publication Policies

Scientific Ethics

Submit a Paper

Usage Permissions



Volume 7
Issue 4
December 2015

Help & Support

[All Issues](#)

About Us

Cookies & Privacy

Wiley Job Network

Terms & Conditions

Find an article

Advertisers & Agents

and

or



Powered by Wiley Online Library Copyright © 1999 - 2016 John Wiley & Sons, Inc. All Rights Reserved

Read the Article

Current Issue

Stay Connected to Eos



[Access Eos Archive Issues](#)

Issues from 1997-2014 are freely available to the public.

Older issues are available through AGU membership or through an institutional subscription.

Journal Resources

[Call for Papers](#)

[Special Section Proposal Form](#)

[Personal Choice](#)

[Wiley Open Access](#)

[Institutional and Funder Payments](#)

[Get RSS Feed](#)

Download the App

New Android App Available!



[Download the JAMES app from the Google Play Store](#)

iOS App for iPad or iPhone



Download the JAMES app from the Apple store



Featured Special Collection

The Max Planck Institute for Meteorology Earth System Model

JAMES Special Issue about the MPI-ESM, its components and the CMIP5 simulations.

Highlights

- Permafrost Area Is Sensitive to Key Soil and Snow Physics
- Modeling Weather over Mountainous Terrain
- Improved Models of Wind Flow over Mountains
- Aerosols Make Cumulus Clouds Brighter, but Shorter Lived

See all »

Upcoming AGU Meetings

Chapman Conference on Currents in Geospace and Beyond

22-27 May 2016
Dubrovnik, Croatia

Chapman Conference on Emerging Issues in Tropical Ecohydrology

5-9 June 2016
Cuenca, Ecuador

Fall Meeting

12-16 Dec 2016
San Francisco

[See all »](#)
